Aerosol Science and Technology, 38:619–638, 2004
Copyright © American Association for Aerosol Research
ISSN: 0278-6826 print / 1521-7388 online
DOI: 10.1080/02786820490479833

Numerical Characterization of Particle Beam Collimation: Part II Integrated Aerodynamic-Lens–Nozzle System

Xuefeng Zhang,[1] Kenneth A. Smith,[1] Douglas R. Worsnop,[2] Jose L. Jimenez,[2]
John T. Jayne,[2] Charles E. Kolb,[2] James Morris,[3] and Paul Davidovits[3]
[1]Department of Chemical Engineering, Massachusetts Institute of Technology,
Cambridge, Massachusetts
[2]Aerodyne Research, Inc., Billerica, Massachusetts
[3]Department of Chemistry, Boston College, Chestnuts Hill, Massachusetts

As a sequel to our previous effort on the modeling of particle motion through a single lens or nozzle, flows of gas–particle suspensions through an integrated aerodynamic-lens–nozzle inlet have been investigated numerically. It is found that the inlet transmission efficiency (η_t) is unity for particles of intermediate diameters ($D_p \sim 30$–500 nm). The transmission efficiency gradually diminishes to ∼40% for large particles ($D_p > 2500$ nm) because of impact losses on the surface of the first lens. There is a catastrophic reduction of η_t to almost zero for very small particles ($D_p \leq 15$ nm) because these particles faithfully follow the final gas expansion. We found that, for very small particles, particle transmission is mainly controlled by nozzle geometry and operating conditions. A lower upstream pressure or a small inlet can be used to improve transmission of very small particles, but at the expense of sampling rate, or vice versa. Brownian motion exacerbates the catastrophic reduction in η_t for small particles; we found that the overall particle transmission efficiency can be roughly calculated as the product of the aerodynamic and the purely Brownian efficiencies. For particles of intermediate diameters, Brownian motion is irrelevant, and the modeling results show that the transmission efficiency is mainly controlled by the lenses. Results for an isolated lens or nozzle are used to provide guidance for the design of alternative inlets. Several examples are given, in which it is shown that one can configure the inlet to preferentially sample large particles (with $\eta_t > 50\%$ for $D_p = 50$–2000 nm) or ultrafine particles (with $\eta_t > 50\%$ for $D_p = 20$–1000 nm). Some of the results have been compared with experimental data, and reasonable agreement has been demonstrated.

INTRODUCTION

In Part I (Zhang et al. 2002), we reported simulation results for the collimation of a particle beam by a single aerodynamic lens or nozzle. In this article, we apply the same numerical method to model the collimation of particle beams by an integrated aerodynamic-lens–nozzle inlet. In brief, the gas flow field in the aerodynamic-lens–nozzle inlet system is calculated by a commercially available numerical package (FLUENT®; Fluent, Inc., Lebanon, NH, USA). For this purpose, the effect of particles on the gas flow is neglected. Particle trajectories are then calculated by integrating the particle momentum equation with the previously calculated flow field as an input. A detailed description of the numerical method, the assumptions, and the error analysis has been provided in Part I. A typical lens–nozzle inlet is analyzed, and the predictions are then compared with experimental results. Further analyses are conducted to characterize the role of inlet upstream pressure in controlling beam performance. Finally, results for the effect of lens geometry and number of lenses on the beam performance are presented, with emphasis on the collimation of ultrafine particles (∼10 nm in diameter). A dimensional analysis of the results, similar to the analysis in Part I, was conducted to provide a general understanding of the mechanisms governing particle beam collimation by the inlet.

In Zhang et al. (2002), the most important performance characteristics of an isolated lens were the particle transmission efficiency and the contraction ratio. The most important performance characteristics of an isolated nozzle were divergence angle and the particle speed. These characteristics were shown to be determined by particle Stokes number (St), flow Reynolds number (Re), and lens geometry. The lens geometry was mainly

---

Received 4 September 2003; accepted 29 April 2004.

This work was supported by EPA grant 82539-01-1.

Xuefeng Zhang is currently with Nano-C, Inc., Westwood, MA 02090.

Jose L. Jimenez is currently with Department of Chemistry, University of Colorado at Boulder, Boulder, CO 80309-0216.

Address correspondence to Kenneth A. Smith, Department of Chemical Engineering, Massachusetts Institute of Technology, 77 Massachusetts Avenue, Room 66-540, Cambridge, MA 02139-4307. E-mail: kas@mit.edu

characterized by ID/OD, the ratio of lens inner diameter to outer diameter (see Part I for details). This article further explores the influence of these parameters on the quality of a particle beam generated by an integrated aerodynamic lens–nozzle inlet. The results will assist in the design of inlets that generate particle beams with high transmission efficiencies over a wide range of particle sizes. This is important for the development of particle measurement instruments equipped with these inlets, because instrument efficiency is largely determined by the inlet transmission efficiency. Obviously, a high particle collection efficiency at a downstream detector requires that the particle beam divergence be very low. Another desirable parameter of the inlet is a high sampling flow rate, because a high flow rate permits the acquisition of reliable particle statistics in a short period.

RESULTS AND DISCUSSIONS

A Typical Integrated Aerodynamic-Lens–Nozzle Inlet

Fundamentals. Figure 1 shows plots for trajectories of particles of 25 nm (Figure 1a), 500 nm (Figure 1b), and 10,000 nm (Figure 1c) diameter in a typical aerodynamic-lens–nozzle inlet. The inlet consists of 5 lenses with inner diameters that are gradually reduced from 5 to 4 mm (5.0, 4.8, 4.5, 4.3, and 4.0 mm). The outer diameter (OD) of the lens is 10 mm. Note that the lenses are thin (0.5 mm) disks except for the first and last lenses, which are cylinders 10 mm in length. The nozzle, which is located at $X = 0$, converges smoothly to a throat diameter of 3 mm (the nozzle is shown schematically in Figure 10b and will be discussed later). It is assumed that the target is a 2 mm diameter plate which is located 240 mm downstream of the nozzle. This target configuration defines a collection half-angle of 4.2×10^{-3} rad (or 4.2 mrad), which is relevant to aerosol measurement instruments that use a thermal desorption process for particle evaporation (Jayne et al. 2000; Tobias et al. 2000). The inlet upstream pressure, P_{up}, is 278 Pa and the downstream pressure, P_{back}, is 0.1 Pa. This back pressure value is typical of the system described by Jayne et al. (2000), and all results presented in this article are based on P_{back} of 0.1 Pa. The 278 Pa upstream pressure yields a predicted flow rate (Q) of 97.3 scc/min, which is quite close to the measured value (100 scc/min; Jayne et al. 2000; more data will be presented later in this article). This value of Q and the tube OD yield a flow Reynolds number, Re_0, of 13.9. It should be noted that, in a real system, a pinhole is added upstream of the inlet to define a fixed flow rate Q. The Q of 100 scc/min discussed here is obtained with a 100 μm diameter pinhole (Jayne et al. 2000). As will be shown later in this article, for an integrated aerodynamic-lens–nozzle system in which flow is choked at the nozzle throat, P_{up} is determined largely by the value of Q. This suggests that in a fixed real system one can adjust P_{up} merely by using a different upstream pinhole. Obviously, flow through the pinhole may also cause particle losses. For convenience, the flow through the pinhole has not been considered in this article.

Note that each trajectory line in Figure 1 represents 10% of the particle flow rate if the particles are distributed uniformly in the flow upstream of the first lens and if the upstream velocity profile is parabolic. The results show that the 25 nm diameter particle beam is quite divergent so that less than 10% of the particles reach the target (plot A), whereas 500 nm diameter particles (plot B) are highly collimated so that the beam size is considerably smaller than that of the target. The particle collection efficiency at the target is therefore unity. For the 10000 nm diameter particles, about 60% of the particles impact on the front surface of the first lens, but almost all the rest of the particles reach the target (see plot C). The beam for particles of this size is seen to be wider than the beam for 500 nm particles but still roughly within the target.

Variations in the axial velocity for particles with diameters of 10, 100, and 10,000 nm are plotted along with the gas velocity in Figure 2. These data pertain to particle or gas elements which enter the inlet near the axis ($R = 0.2$ mm). For reference, the inlet geometry is also included in the figure. As expected, the gas is accelerated and decelerated while passing through each lens. The gas speed reaches a maximum value of 600 m/s a little downstream of the nozzle and then diminishes quickly in the further expansion of the gas. It is observed that the 10 nm diameter particle very closely follows the gas velocity in each acceleration and deceleration step, except at the final expansion to vacuum, where the particle was accelerated to only about 400 m/s and then shows a minor decline to a final velocity of about 385 m/s in the very low pressure, slowly moving gas. By contrast, particles with a diameter of 100 nm were accelerated and decelerated slightly less effectively at each lens step, but they still attained the gas speed in each of the spaces between lenses. A feature of particles of this size is that the velocity attained in the region immediately downstream of the final nozzle does not exhibit an overshoot. Particles with a diameter of 10,000 nm do not follow the gas at all, and the final velocity is only about 40 m/s. Figure 2 also shows that the gas pressure drops at each lens, but most of the pressure drop (~2/3 of total) is at the nozzle. If the number of lenses were increased, the inlet upstream pressure at a fixed Q would be correspondingly increased.

Liu et al. (1995a, b) have shown that, for small particles ($D_p < 50$ nm), Brownian motion plays an important role in broadening the particle beam. Their pioneering work showed that the angular particle distribution function due to Brownian motion of particles emanating from a point source can be expressed as

$$f(\alpha) = \frac{2\alpha}{{\alpha_B}^2} \exp\left[-\left(\frac{\alpha}{\alpha_B}\right)^2\right], \qquad [1]$$

where

$$\alpha_B = \sqrt{\frac{2kT_g}{m_p}}\frac{1}{U_p}, \qquad [2]$$

m_p is the particle mass, T_g is the gas temperature, k is Boltzmann's constant, U_p is the particle axial terminal velocity, and α is the divergence angle (defined as the half-angle of the cone). For this distribution function, it is possible to calculate the collection

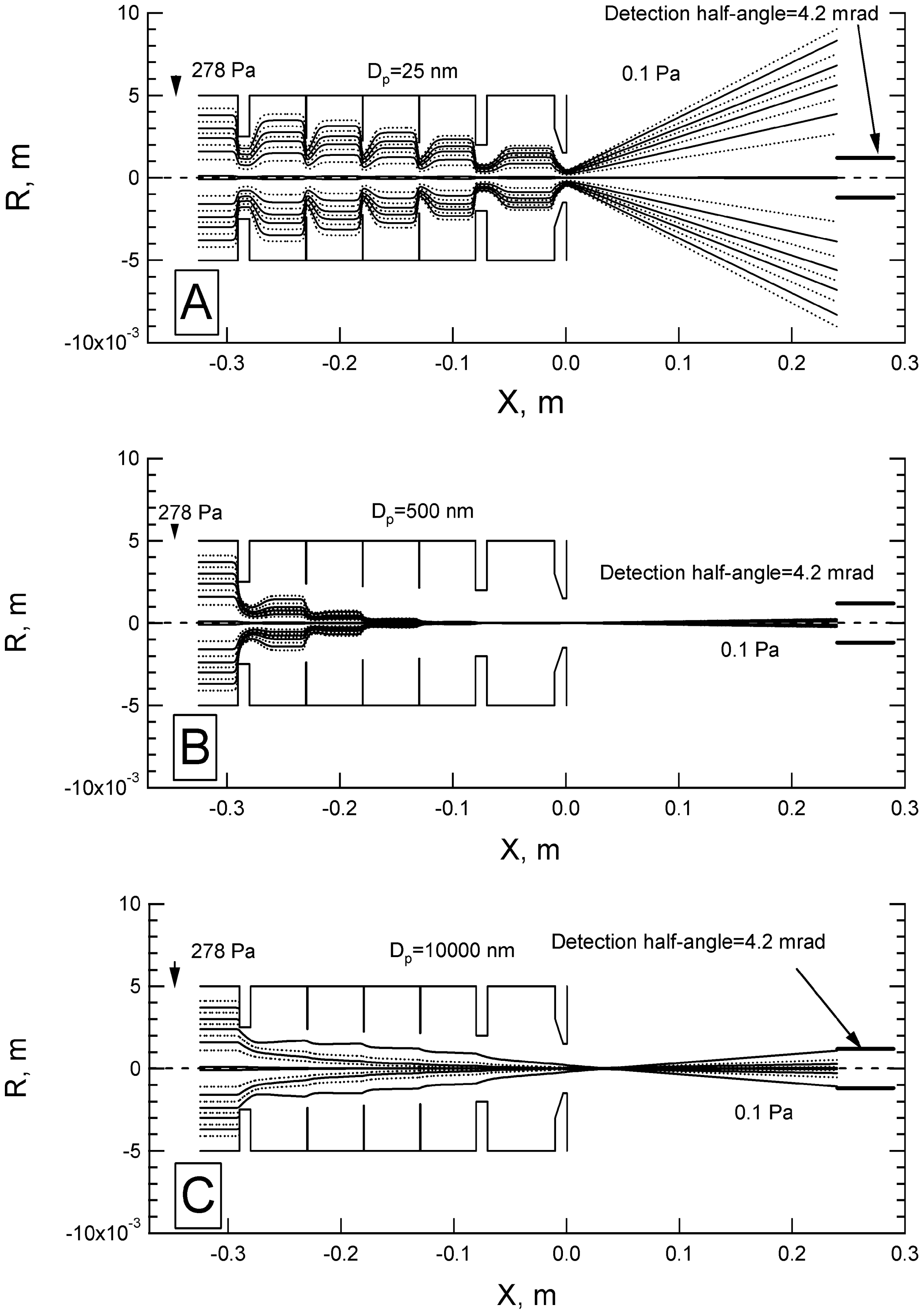

Figure 1. Trajectories of 25 nm, 500 nm, and 10000 nm diameter particles in a typical inlet. $P_{up} = 278$ Pa, $P_{back} = 0.1$ Pa, $Q = 97.3$ scc/min, OD = 10 mm, $Re_0 = 13.9$. IDs are 5*, 4.8, 4.5, 4.3, and 4.0* mm. The space between lenses is 50 mm. Smooth nozzle (shown in Figure 10a). All lenses are thin (0.5 mm) disks except for the first and last lenses (with * above) which are cylinders 10 mm in length.

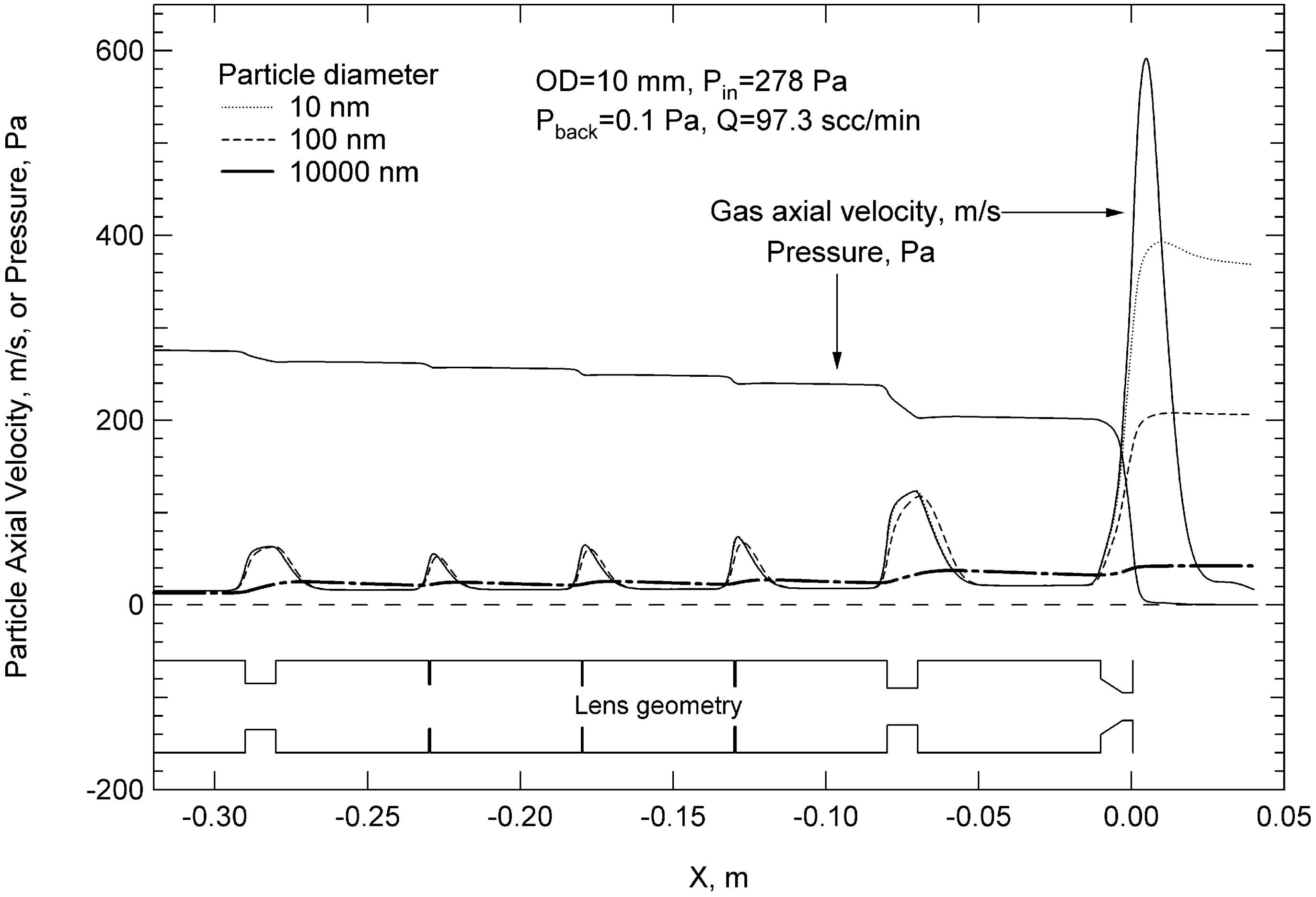

Figure 2. The same inlet as in Figure 1, plot of axial velocity of particles (D_p = 10, 100, and 10000 nm) and of gas; gas pressure is also plotted.

efficiency within an angle α_{det}. Liu et al. (1995a, b) showed that 90% of the particles will lie within an angle given by $3.04\alpha_B$. The choice of gas temperature, T_g, is complicated by the fact that particle Brownian motion is the result of collisions with gas molecules just upstream of the very low pressure region. In the expansion through the final nozzle, Fluent predicts gas temperatures in the range of 273–150 K. In the present calculations, T_g was chosen as 273 K, so the results define the upper limit of the Brownian effect.

By analyzing particle trajectories like those shown in Figure 1, one can obtain the divergence angle versus particle diameter for purely aerodynamic collimation. Figure 3 shows the beam angle that encloses 90% of the particles for inlet upstream pressures of 320 Pa ($Q = 121$ scc/min, resulting in $Re_0 = 17.3$, circles) and 67 Pa ($Q = 9.49$ scc/min, resulting in $Re = 1.35$, squares) for the inlet shown in Figure 1. Figure 3 also shows the same angle due to Brownian broadening (nearly straight solid and dashed lines). For simplicity, the Brownian broadening angles shown in the figure are for those particles that originate on the axis of the nozzle. Brownian broadening of off-axis particles will be discussed later.

In Figure 3, both the circles and the squares show that aerodynamic beam angles are relatively large for both very small and very large particles. For particles of intermediate size, collimation is good and the aerodynamic divergence angle exhibits minima at three separate particle sizes. To aid in the understanding of these results, trajectories of particles of different sizes, but with a fixed upstream radial coordinate of 2.5 mm, are plotted in Figure 4. These are computed for the case $P_{up} = 320$ Pa ($Q = 121$ scc/min).

Figure 4 shows that, for very small particles (e.g., D_p = 25 nm), the beam is highly divergent. This is because particles with such small inertia follow the gas closely. Consequently, the divergence angle shown in Figure 3 is large when D_p is small. As particle size increases, the particle beam becomes less divergent (particle motion is more distinct from gas motion, e.g., D_p = 50 nm). For even larger sizes, another mode of behavior appears in which particles cross the axis at a position downstream of the nozzle (D_p = 100 nm). This transition leads to the first minimum in Figure 3. With further increases in particle size, the particle beam is better collimated by the inlet so that the angle associated with axis-crossing is smaller (see D_p = 200 nm in

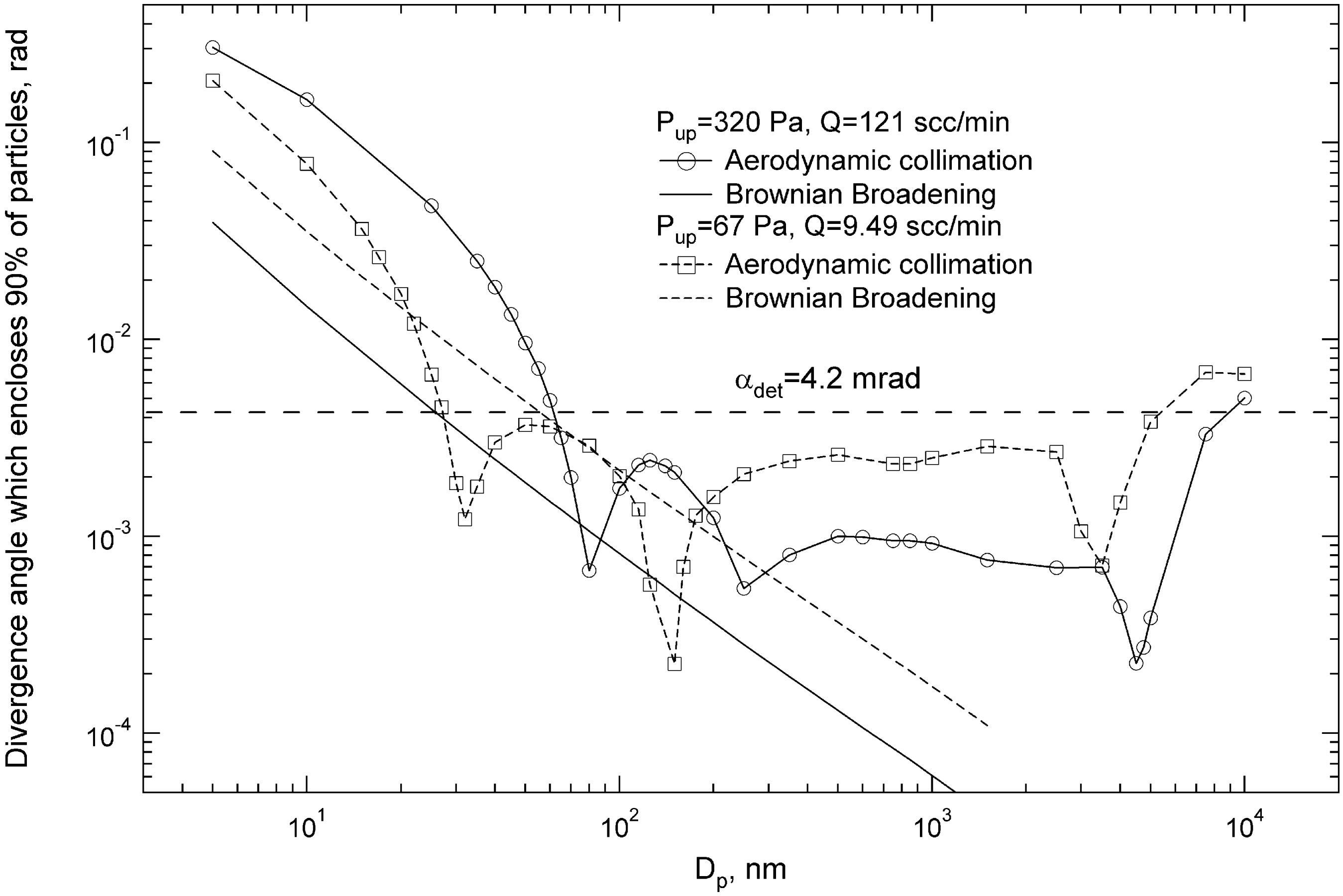

Figure 3. Beam divergence angle enclosing 90% of the aerodynamically collimated particles as a function of particle diameter, Q = 121 scc/min (P_{up} = 320 Pa, Re_0 = 17.3) and Q = 9.49 scc/min (P_{up} = 67 Pa, Re_0 = 1.35); and beam divergence angle enclosing 90% of the particles based solely on Brownian broadening. The same inlet as in Figure 1.

Figure 4). Still larger particles are even better collimated by the lenses and eventually the particle motion evolves into another mode in which the trajectories cross the axis twice, first downstream of the last lens and then in the vicinity of the nozzle (see D_p = 350 nm in Figure 4). The transition generates the second minimum in Figure 3. For very large particles—for instance, D_p = 10,000 nm—the particle motion reverts to a mode with a single axis crossing but with a much higher angle. This leads to the last minimum in Figure 3 at $D_p \sim 4000$ nm.

The squares in Figure 3 are for P_{up} = 67 Pa (Q = 9.49 scc/min). These show much the same trends as the circles but are shifted to smaller sizes. In other words, at lower pressures smaller particles are collimated more effectively but larger particles are collimated less effectively. This is mainly due to the fact that the particle Stokes number is roughly proportional to D_p/P_{up} (see Zhang et al. 2002, Equation (7), for details). The actual shift in D_p is less than this would suggest because viscous effects are considerably more important at the lower flow rate. More discussion on the effect of upstream pressure on beam performance will be provided later in this article.

As stated earlier, Brownian broadening of an idealized, perfect beam is used to estimate broadening by Brownian motion. The nearly straight solid line (P_{up} = 320 Pa) and the nearly straight dashed line (P_{up} = 67 Pa) in Figure 3 enclose 90% of the particles for such idealized beams. The figure shows that the purely Brownian angles for P_{up} = 320 Pa are lower than those for P_{up} = 67 Pa. This is merely because higher values of P_{up} result in higher values of particle terminal velocities, and Brownian motion therefore has less time to broaden the particle beam. The dotted horizontal line in Figure 3 provides a reference at an angle of 4.2 mrad. This represents a typical collection angle for instruments that use thermal desorption detection (Jayne et al. 2000; Tobias et al. 2000). The figure shows that for P_{up} = 320 Pa and 60 nm $< D_p <$ 8000 nm, the divergence angle is always smaller than that required. Furthermore, Brownian broadening is generally not important in this case. For the P_{up} = 67 Pa condition, however, the aerodynamic collimation angle (the squares) and the Brownian broadening angle (the dashed line) are comparable over a wide range of D_p. One would therefore expect Brownian broadening of the overall beam to be significant.

From Equations (1) and (2), it might be expected that the slope of the Brownian broadening lines in Figure 3 would be about −1.5. In other words, for constant U_p (particle terminal velocity), the angle would vary as the inverse square root of

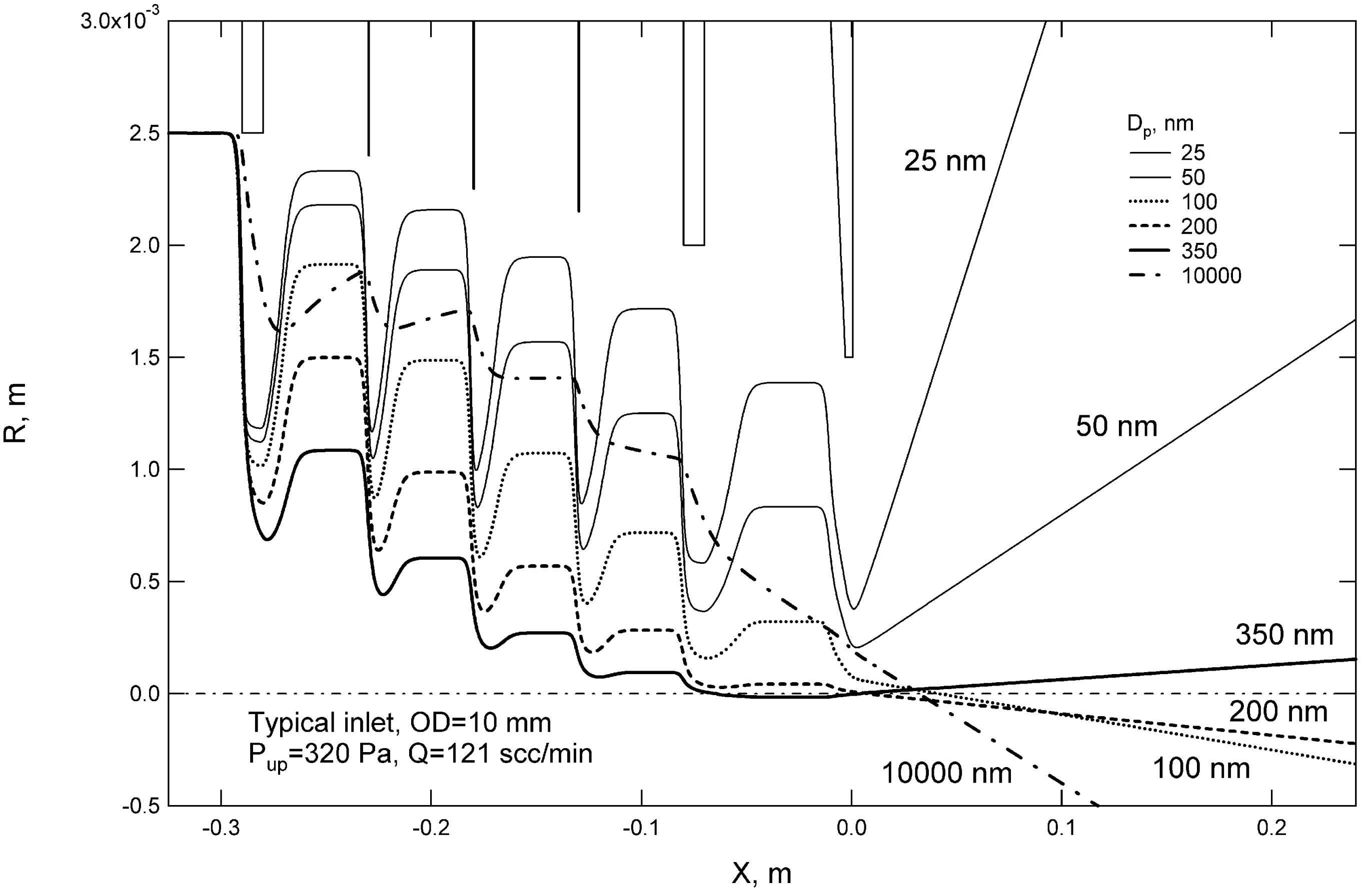

Figure 4. Trajectories of particles of various diameters. $P_{up} = 320$ Pa (121 scc/min, $Re_0 = 17.3$), $R_{pi} = 2.5$ mm. The same inlet as in Figure 1.

the mass of the particle. However, U_p is not independent of D_p, but instead decreases with D_p. As a result, the Brownian broadening lines in Figure 3 have slopes in the vicinity of -1.2. For extremely small particles, the dependence of U_p upon D_p is particularly weak, and this is the explanation for the observed curvature of the Brownian broadening curves.

Figure 5 presents the corresponding results for the transmission efficiency, which is defined as in Zhang et al. (2002) i.e., the fraction of the particles reaching the target relative to the number of particles at the inlet upstream. The collection angle is taken to be 4.2 mrad. For the purely aerodynamic case, transmission is poor for very small particles ($D_p \cong 15$ nm) because, for this operating pressure, the divergence angle is large. Transmission efficiency improves as D_p increases, and it reaches unity at D_p about 25 nm, which roughly corresponds to the D_p at which the squares cross the dotted line ($\alpha = 4.2$ mrad) in Figure 3 (even though the results in Figure 3 are for a beam that encloses 90% of the particles, the results for a beam that encloses 100% of the particles are quite similar for the case of purely aerodynamic broadening). As discussed in Zhang et al. (2002), the monotonic reduction in transmission efficiency for $D_p > 600$ nm is largely due to impact losses on the front lens.

The dashed line in Figure 5 is for transmission of an ideal beam as determined solely by Brownian broadening. It follows from Equation (1) for the case of $\alpha_{det} = 4.2$ mrad. It has been applied only to those particles located on the axis of the nozzle. For $D_p < 50$ nm, the transmission efficiency for Brownian broadening is considerably lower than that for purely aerodynamic collimation. Thus Brownian motion will have a large impact on overall inlet transmission efficiency for these small particles.

So far, the Brownian broadening calculation has been applied only to those particles that are originally on the beam axis. In order to obtain the angular distribution function of a beam, however, one needs to consider Brownian motion of off-axis particles and the aerodynamic angular distribution. Fortunately, the aerodynamic distribution and the Brownian distribution are not physically coupled. The procedure adopted, therefore, was to first calculate the aerodynamically determined distribution function. All particles in this purely aerodynamic beam were then subjected to Brownian motion. For particles at a certain coordinate in the purely aerodynamic beam (no Brownian motion included), Equation (1) can be used to predict subsequent spread due to Brownian motion. Brownian broadening upstream of the nozzle exit was neglected. Integration over all particles

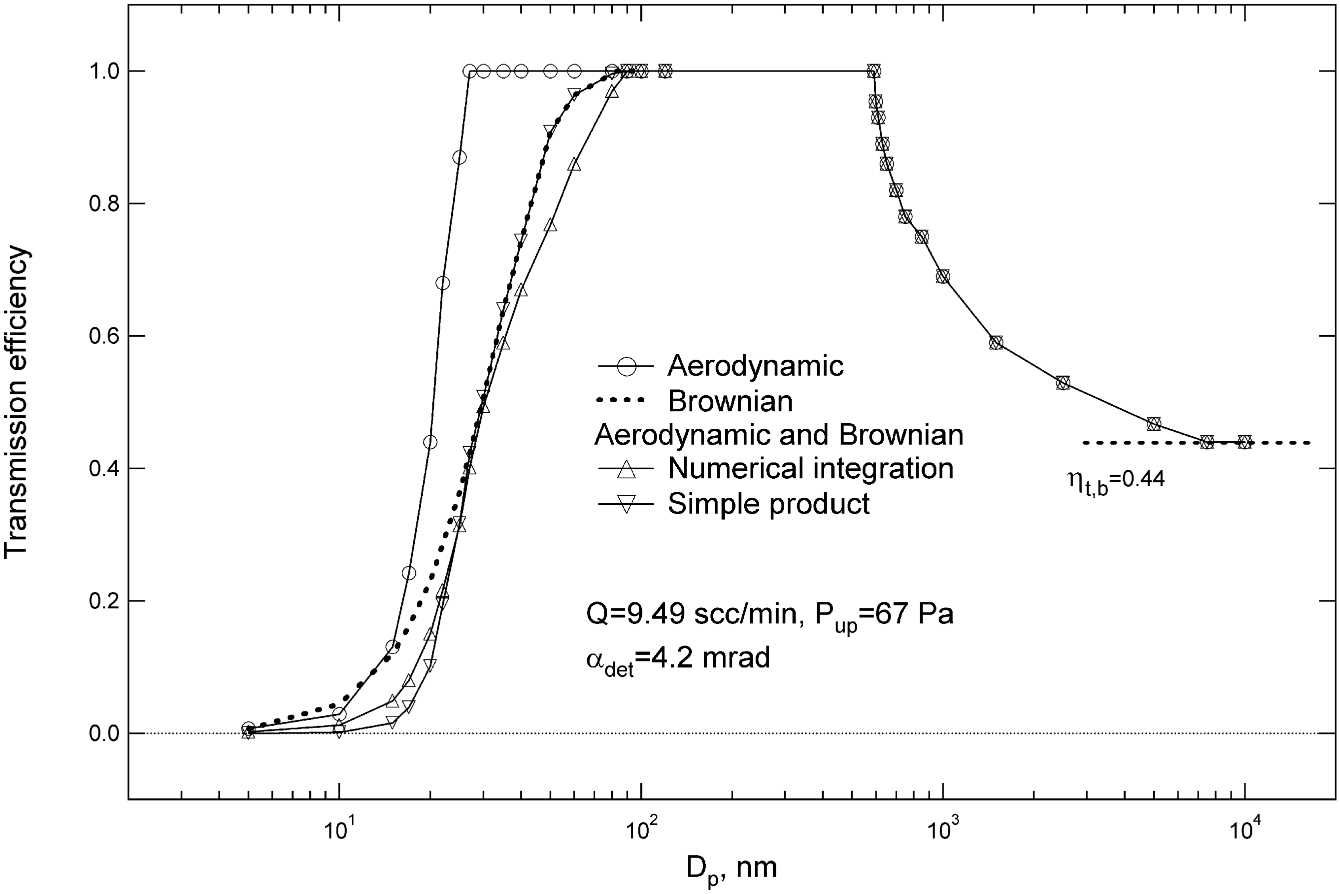

Figure 5. Particle transmission efficiency versus particle diameter for purely aerodynamic collimation, Brownian broadening, and both. $\alpha_{\text{det}} = 4.2$ mrad. The same inlet as shown in Figure 1 ($\text{Re}_0 = 1.35$).

in the aerodynamically collimated beam yields the angular distribution function of the final beam. The calculation has been conducted numerically, and representative results are shown in Figure 5 (upward pointing triangles). For example, for 50 nm particles it is no surprise that the overall particle transmission efficiency obtained from the numerical calculation is lower than the efficiency obtained from Brownian broadening of particles perfectly collimated to the axis (dashed line). This is because Brownian motion of particles initially located near the edge of the aerodynamically collimated beam leads to a net loss of particles to regions outside the capture angle. The upside-down triangles in the figure are obtained simply by multiplying the efficiencies for the two idealized cases (circles and the dashed line). Figure 5 shows that the upside-down triangles provide an imperfect, but reasonable, approximation to the overall transmission efficiency obtained by numerical integration. Therefore, the product of transmission efficiencies from aerodynamic collimation and Brownian motion is used in the remainder of this article to represent inlet overall transmission efficiency.

Operation of Inlet at Different Upstream Pressures. It was shown in Zhang et al. (2002) that three dimensionless parameters (flow Reynolds number, particle Stokes number, and lens ID/OD) have large impacts on the performance of isolated lenses or nozzles. It is reasonable to expect that the performance of an integrated inlet will also be controlled by the same three dimensionless parameters. We would like first to investigate the effect of Re and St on the performance of an integrated inlet. In Zhang et al. (2002), upstream pressure and the flow rate of an isolated lens could be specified independently. However, for a choked nozzle, and therefore for an integrated system, the upstream pressure and the flow rate are directly related, so the two are not independent.

Both modeling and experimental efforts have been undertaken to characterize particle beam performance as a function of Re and St. The experimental setup and procedure are described in detail by Jayne et al. (2000). Only a brief description is provided here for convenience. In the experiments, an atmospheric pressure gas–particle suspension passes through a pinhole (~100 μm), which controls the inlet mass flow rate (~100 scc/min). Measurements of particle transmission efficiency and terminal velocity were obtained as a function of particle diameter by sampling nominally monodisperse particles that were preselected by a differential mobility analyzer (DMA; model 3032, TSI, St Paul, MN, USA). The inlet particle concentration was monitored by a condensation particle counter (CPC; model 3022A, TSI, St Paul, MN, USA). Unfortunately, the DMA does not quite select a monodisperse population of particles because large multiply charged particles behave like small singly charged particles. For this reason, a model has been developed to convert the CPC-DMA readings to the true size distribution of particles in the sample; see Jayne et al. (2000). The mass distribution versus diameter for several pure materials (oleic acid, NH_4NO_3 and dioctyl phthalate) was measured by a quadrupole mass spectrometer located downstream of the inlet, and the results were compared with the inlet particle mass distribution function derived from the corrected CPC-DMA readings. The result provides a measure of particle transmission efficiency as a function of diameter. Particle terminal velocity was measured directly by using a mechanical chopper to determine the particle time-of-flight over a known flight path (395 mm). It should be noted that the OD in the real inlet was 8.8 mm for machining convenience, and this is slightly smaller than that used in Figures 1–5 (10 mm). This difference in OD does not alter the trends shown in Figures 1–5.

Figure 6 is a plot of dimensionless gas mass flow rate versus gas flow Reynolds number for the real inlet. Because the flow rate is controlled by choked flow through the nozzle, the Reynolds number here is expressed in terms the sonic speed C_0 and the nozzle OD. Both the sound speed and the gas properties are evaluated at upstream conditions. This choice is solely for convenience. The difference in the two pressures is less than 30% (see Figure 2). The dimensionless flow rate is defined as the mass flow rate predicted by the FLUENT model divided by the prediction of a simple isentropic one-dimensional calculation. The mass flow rate through a nozzle for a one-dimensional model is well known and is given, for instance, by Shapiro (1953):

$$Q_{1D} = \frac{P_{up}A^*}{\sqrt{T_{up}}}\sqrt{\frac{\gamma}{R}\left(\frac{2}{\gamma+1}\right)^{\frac{\gamma+1}{\gamma-1}}}, \quad [3]$$

where A^* is throat area of a nozzle, R is the gas constant and $\gamma = 1.4$ for air. In Figure 6, the solid line is for the model results and the squares are experimental data measured by pressure gauges and a flow meter. In the experiments, pinholes of two diameters were used: 100 μm, for which Re is around 200, and 70 μm, for which Re is around 80. The results show that the dimensionless mass flow rate varies monotonically with flow Reynolds number, and reasonable agreement is observed

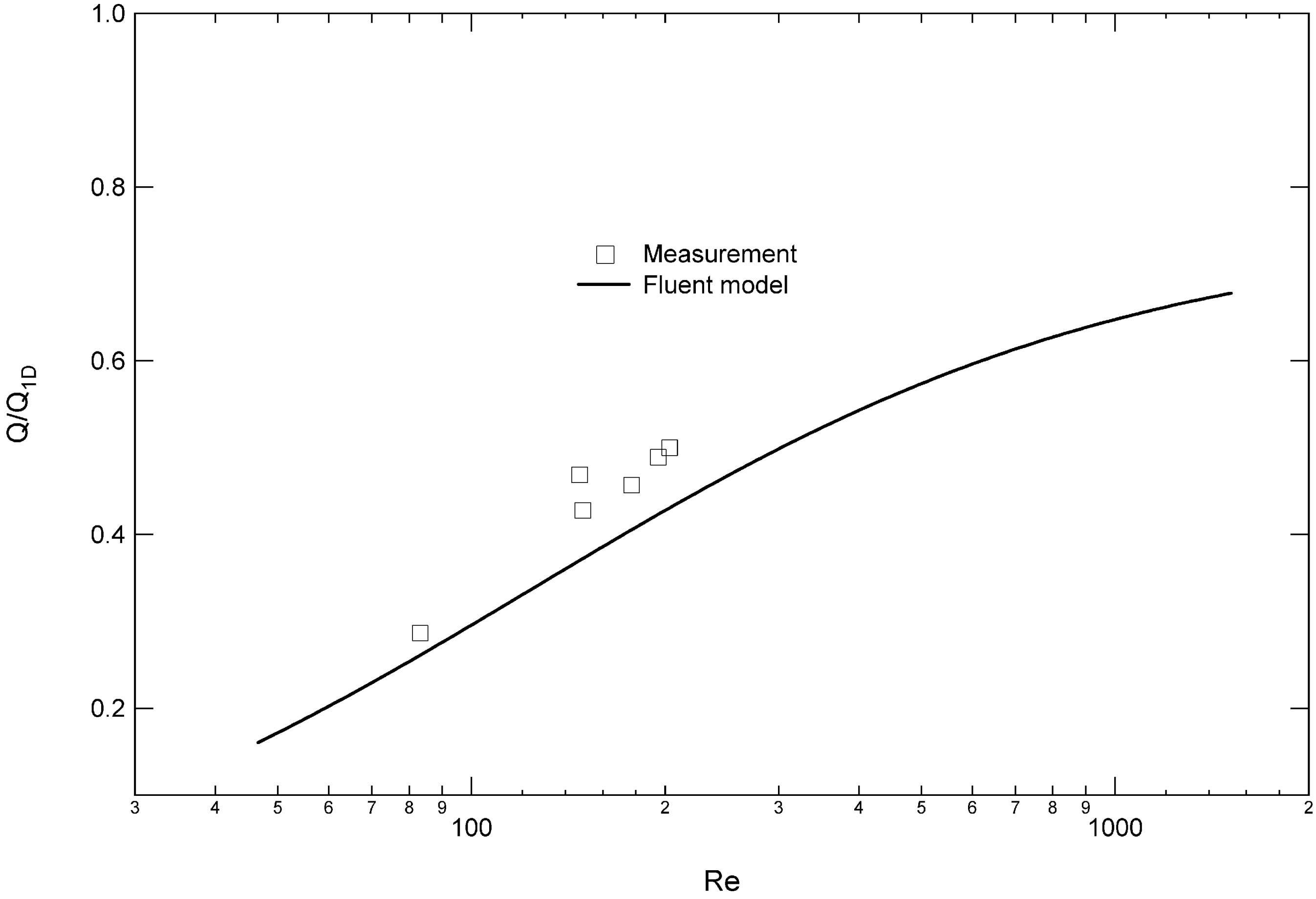

Figure 6. Gas mass flow rate normalized by one-dimensional calculation (Equation (3)) versus flow Reynolds number which is based on inlet OD and gas sonic speed upstream of the inlet. The same inlet as shown in Figure 1, except for OD = 8.8 mm.

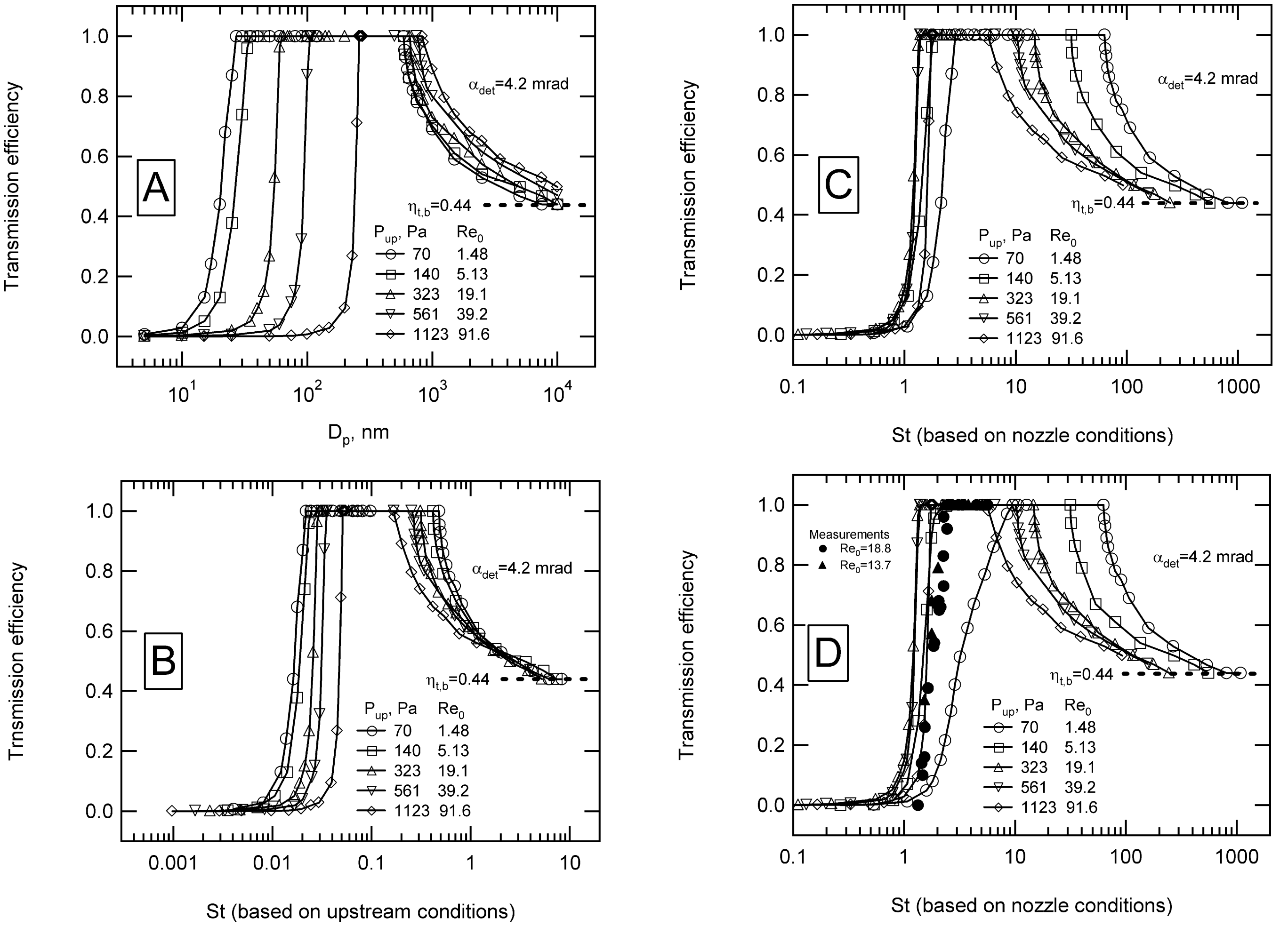

Figure 7. Particle transmission efficiency at different flow rates (upstream pressures), $Re_0 = 1$–100. $\alpha_{det} = 4.2$ mrad; (a) purely aerodynamic transmission versus particle diameter; (b) purely aerodynamic transmission versus St based on inlet upstream pressure, gas velocity, and ID of first lens; (c) purely aerodynamic transmission versus St based on inlet upstream pressure, sonic speed upstream of the inlet, and nozzle throat diameter; (d) the same as (c) but with inclusion of Brownian beam broadening mechanism and experimental data. The same inlet as shown in Figure 1 except for OD = 8.8 mm.

between the model and the experimental data. This trend is similar to that found by Shapiro (1953) for a sharp-edged orifice, in which case the Re dependency was explained as a consequence of a thinner boundary layer at higher Re. Note that, at the highest value of Re, the ratio of Q/Q_{1D} would be about 1.0 if the pressure immediately upstream of the nozzle had been used to compute Q_{1D}.

Because the experimental data on transmission efficiency were obtained with two different pinholes, and therefore at two different Reynolds numbers, it is useful to explore the effect of pressure on transmission efficiency. Figure 7a is a plot of particle transmission efficiency (purely aerodynamic collimation) versus particle diameter for different gas upstream pressures. The figure shows that all curves shift to larger values of D_p with higher P_{up}, as in the single lens/nozzle results of Zhang et al. (2002).

In Zhang et al. (2002) it was shown through dimensionless analysis that particle collimation by a single isolated lens or by an isolated nozzle is a function of particle Stokes number and flow Reynolds number. In the calculation for an integrated inlet, we have chosen to define the flow Reynolds number in terms of parameters that are evaluated just upstream of the inlet, just as in Zhang et al. (2002) for an isolated lens or nozzle. For an integrated inlet, however, the selection of scales to define St is less obvious. To test sensitivity to the choice of scales, we have used both a St based on conditions upstream of the first lens and a St based on conditions upstream of the nozzle.

Figure 7b presents the same results as in Figure 7a but plotted versus St based on inlet upstream conditions (average velocity, P_{up}, first lens ID). For $St \geq 1$, this choice of scales is seen to produce nearly universal behavior; but the same is not observed for very small particles. The near universality for large particles presumably reflects the fact that most particle loss is due to impact on the upstream face of the first lens; and this is the site chosen for scaling.

Conversely, the behavior of very small particles can be expected to be controlled largely by the nozzle. Therefore, in order to describe the behavior of these particles, St should be based on parameters that are characteristic of conditions at the nozzle (local sound speed, nozzle throat diameter, etc.). As in the flow rate calculation, upstream conditions have instead been used to calculate the sound speed and the physical properties. This is for convenience and is permissible only because upstream conditions and nozzle conditions are not very different. As shown Figure 7c, these selections provide a more nearly universal correlation between Stokes number and transmission efficiency for very small particles.

Figure 7c shows that the small particle cutoff of the transmission data is located approximately at St ≈ 1, except for the case of $P_{up} = 70$ Pa (Q = 9.09 scc/min, $Re_0 = 1.48$). As expected, the roughly universal dependence suggests that, for very small particles, the nozzle is the controlling unit in the inlet. This also implies that one could adjust the cutoff D_p (i.e., the value of D_p at which η_t becomes essentially zero) by adjusting nozzle geometry and/or operating conditions. The minor deviations in the location of the cutoff in Figure 7c are due to differences in the flow Reynolds number (over the range of 1–100). Figure 7d is for the same situation as in Figure 7c but Brownian dispersion has been included. It is seen that only the curve for $Re_0 = 1.48$ is significantly changed. Figure 7d also shows reasonable agreement with the experimental data at two conditions, $Re_0 = 18.8$ and 13.7. The significance of the results in Figure 7 is that one can use a Stokes number based on conditions at the nozzle to estimate particle cutoff at small sizes, and a Stokes number based on conditions at the first lens to estimate impact losses at large sizes. In both cases, the criterion is simply St ~ 1, but it is essential that St be appropriately defined.

Particle final velocity for several values of P_{up} is plotted in Figure 8 as U_p/C_0 versus particle Stokes number based on nozzle parameters (as in Figure 7d). The figure shows that higher Re leads to a higher particle final velocity. Experimental data ($Re_0 = 18.8$ and 13.7) are seen to be in good agreement with the model prediction. As Brownian broadening is inversely proportional to the axial velocity of the particle, one way to reduce Brownian broadening is to operate at high Re and low St.

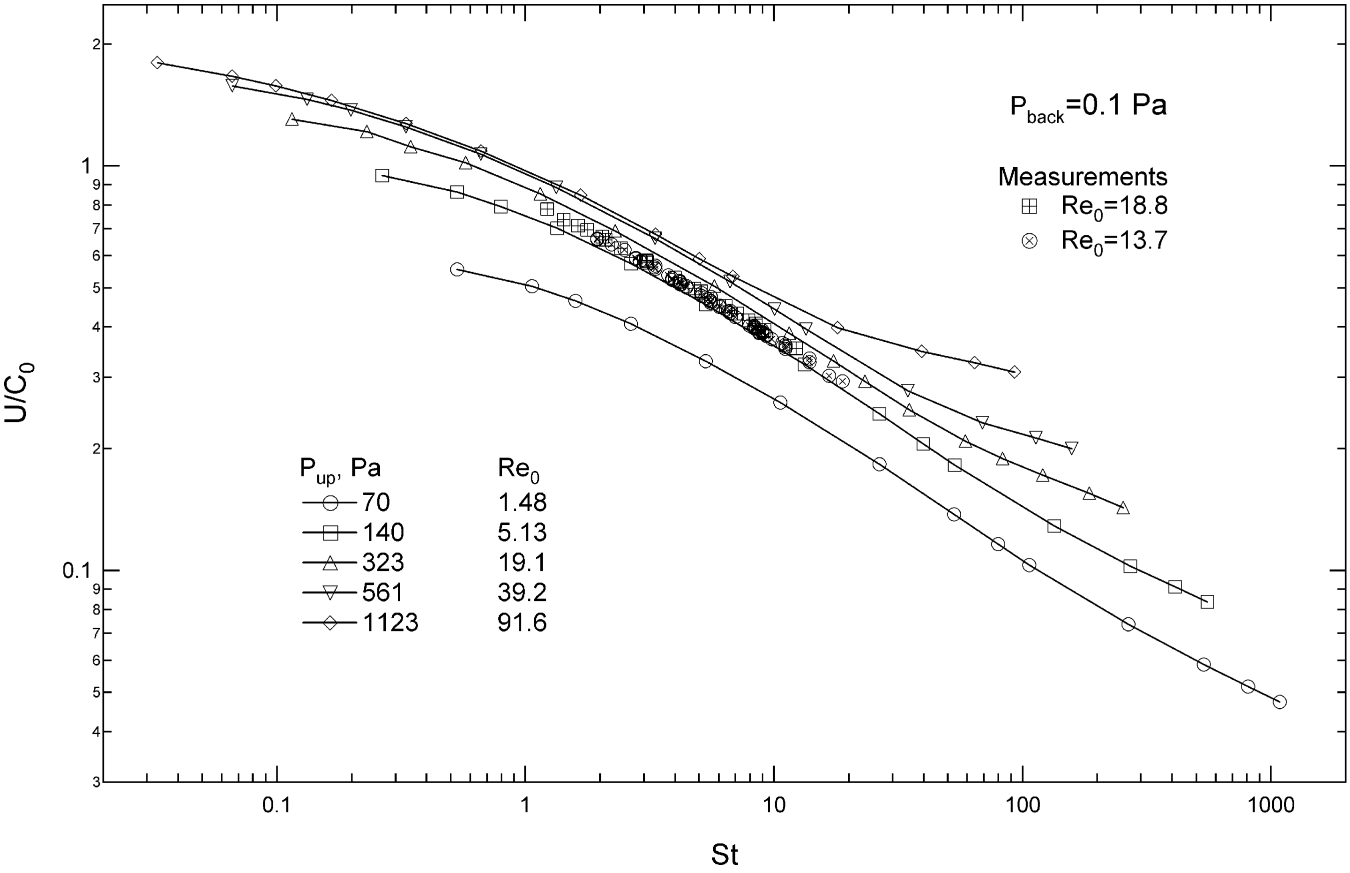

Figure 8. Particle terminal velocity versus diameter for five flow rates or pressures. The same inlet as for Figures 5, 6, and 7. Comparison with experimental data. C_0 is the sonic speed evaluated at conditions upstream of the inlet. St is based on inlet upstream pressure, C_0, and nozzle throat diameter.

The reader may have noticed that the values of Re and St given here are not consistent with the values cited in Zhang et al. (2002). The values of Re and St quoted in Zhang et al. (2002) are consistently too high by a factor of 1.1*(4/3). The dependent variables presented in Zhang et al. (2002), such as transmission efficiency, are correct. The error arises from two sources. The first was an erroneous assumption that the average velocity reported by FLUENT is the mass average velocity. In truth, it is that velocity which, when multiplied by the mass flow rate, will give the momentum flow rate. For a parabolic velocity profile in a circular tube, this velocity is higher than the mass average value by a factor of 4/3. The additional 10% error is entirely of our doing. All values of Re and St presented in this article are believed to be reliable as is; and all results in Part I are believed to be correct if St and Re are divided by 1.1*(4/3).

Effect of Lens and Nozzle Geometry on Particle Beam Collimation

The prior sections of this article are intended to provide an understanding of an inlet of the sort that has typically been constructed (Jayne et al. 2000; Liu et al. 1995a, b). The subsequent sections are intended to explore the design space in a more general way. The inlet OD is fixed at 10 mm, α_{det} is 5 mrad, and Q is 97 scc/min unless specified otherwise. It should be noted that Q for these simulations is not exactly 97 scc/min, because it was matched by adjusting P_{up} until the computed flow was within 1% of that value. These default parameters are slightly different from those which characterize the inlet discussed by Jayne et al. (2000).

Number of Lenses and Nozzle Shapes

In the integrated aerodynamic-lens–nozzle inlet, the nozzle is the unit that finally generates the particle beam. From the single nozzle calculations (Zhang et al. 2002), it is known that the beam divergence angle of any particular particle is roughly proportional to the initial radial position of that particle. Therefore, for a nozzle to generate a particle beam of acceptably small divergence ($<\alpha_{\text{det}}$), the particles must first be collimated by the lenses so that they lie in a region close to the axis. The single nozzle analysis of Zhang et al. (2002) shows that, for a particle with a dimensionless initial radial coordinate of 0.1, the value of the divergence angle for $D_p = 15$–10,000 nm is 0–10^{-2} rad. This implies that, in order to get unit transmission efficiency over the range of $D_p = 15$–10,000 nm with a detection angle of 5 mrad, one needs to collimate all of the particles to a dimensionless radial position of about 0.05 or less.

As shown by Liu et al. (1995a, b), the total lens contraction factor for a particle beam that passes through a series of lenses is approximately the product of the contraction factors for the individual lenses, or

$$\eta_c = \eta_{c1} \times \eta_{c2} \times \eta_{c3} \ldots\ldots \eta_{cn} = \prod_{i=1,n} \eta_{ci}. \qquad [4]$$

This assumes that upstream lenses do not influence the behavior of downstream lenses, i.e., that the separation distance is sufficient to assure independence. Here the beam contraction factor is defined as the downstream radial position of a particle divided by the upstream radial position of the same particle; see Liu et al. (1995a, b) and Zhang et al. (2002). Based on Equation (4), a five-lens inlet will produce the required overall contraction coefficient of 0.05 if the individual lenses each have a contraction coefficient of 0.5, i.e., $(0.5)^5 \cong 0.03$. The single lens results shown in Figure 9 of Zhang et al. (2002) suggest that, for lenses operated at Q = 97 scc/min, a reasonable choice of ID/OD is 0.4 for which $\eta_{ci} = 0$–0.5 for St = 0.1–10, so the design requirement can be satisfied. It is reasonable to expect that one can enhance beam contraction by simply using more lenses. We will first explore this approach.

Figure 9 is a plot of particle transmission efficiency (after considering Brownian motion) versus particle diameter for inlets of 3–5 lenses. The transmission efficiency for the Brownian limit is also plotted for reference. Note that the inlet OD is 10 mm and that the lens (thin disk) IDs were linearly reduced from 5 to 4 mm from the first lens to the last one. A schematic of the nozzle is shown in Figure 10a with $d_n = 3$, $d_t = 6$, and L = 10 mm. This nozzle design was found to have optimal performance in terms of divergence angle in Zhang et al. (2002; Figures 14–16). For reference, the values of P_{up} that produce the required match for Q are noted in Figure 9. Obviously, the individual lenses operate between P_{up} and the nozzle upstream pressure (150 Pa for Q = 97 scc/min) and the lens Re_0 is about constant at 13.9. The figure shows that all curves start from almost zero transmission for D_p less than about 15 nm (the low D_p cutoff) and approach the Brownian limit at a D_p about 20 nm. The purely aerodynamic performance is therefore nearly perfect at $D_p \sim 20$ nm; this was explained earlier as a transition from the absence of axis crossing to the presence of axis crossing just downstream of the nozzle. Clearly, if one wants to shift the low D_p cutoff, one must change the nozzle geometry or the nozzle operating condition, but not the lens parameters.

It is observed in Figure 9 that, for all inlets equipped with a stepped nozzle (Figure 10a), there is a valley at a D_p of about 40 nm, in addition to the severe cutoff at $D_p \sim 15$ nm. The figure also shows that there is a drop in transmission efficiency for large particles. The initial drop at $D_p \sim 300$ nm is due to impact losses on the lenses, but the values that are lower than the ballistic limit arise from poor collimation by the lenses. The figure further shows that, by increasing the number of lenses, the valley at 40 nm is much diminished and the extent of departure from the ballistic limit is less significant.

It is interesting to note that all of the results for individual lenses in Zhang et al. (2002; Figures 5–10) indicate that a lens produces good collimation for particles of intermediate diameter (St = 0.05–5), but poor collimation for small (St < 0.05) and large particles (St > 5). Specifically, one can estimate from the results of Zhang et al. (2002) that, for a lens of ID/OD = 0.4 operated at $P_{\text{up}} = 200$ Pa, $\eta_{ci} = 0$–0.5 at

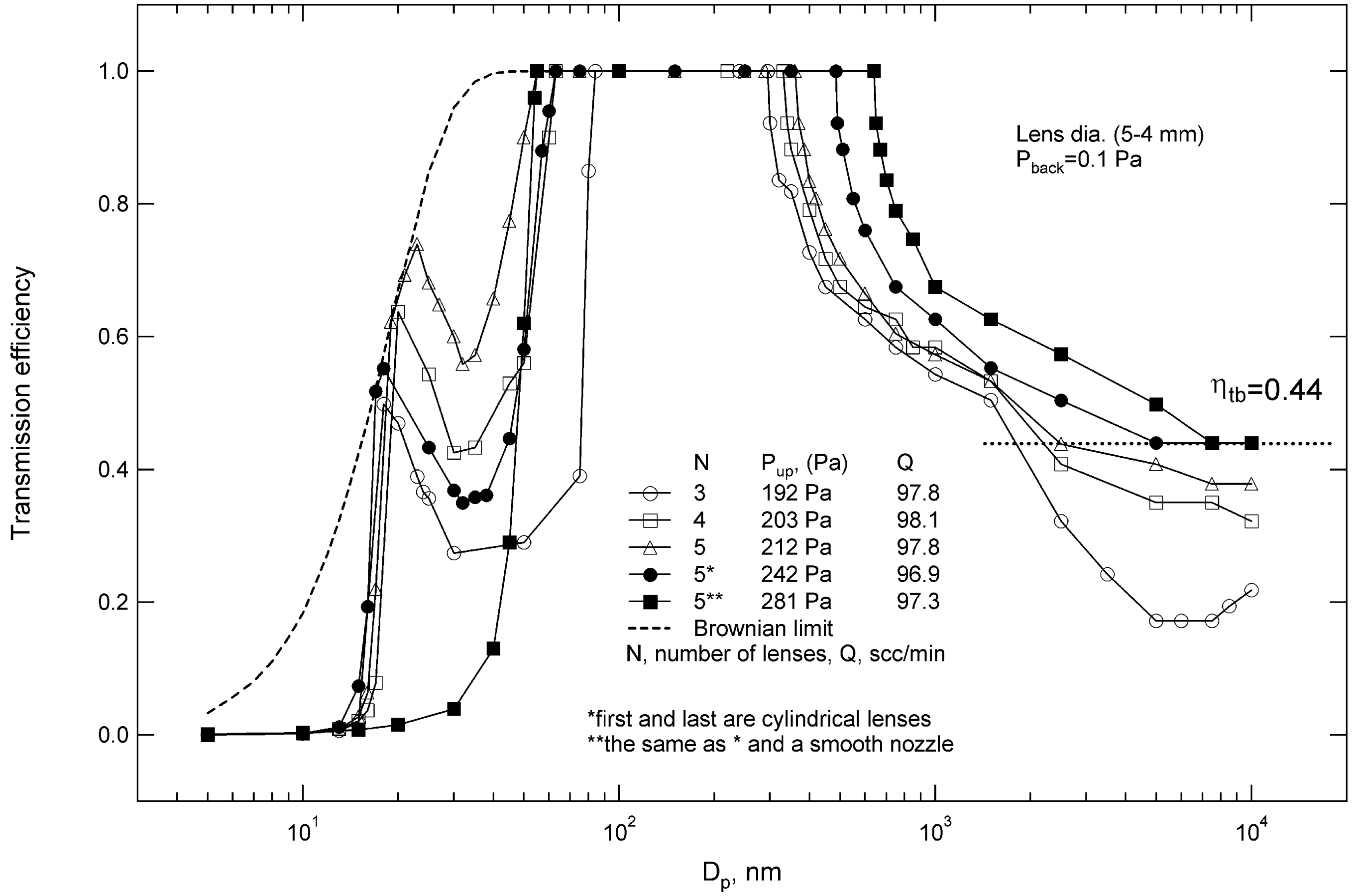

Figure 9. Influence of the number and type of lens as well as nozzle shape on particle transmission efficiency. Q = 97 scc/min, OD = 10 mm, $P_{back} = 0.1$ Pa, $Re_0 = 13.9$, and $\alpha_{det} = 5$ mrad. Thin disk lenses (0.5 mm), except those noted with *, which are 10 mm in thickness.

$D_p = 70$–7000 nm. In other words, the lens may not be effective for $D_p < 70$ and $D_p > 7000$ nm. Fortunately, the nozzle results plotted in Figure 14 of Zhang et al. (2002) show that an isolated nozzle has quite good performance for small ($D_p = 15$–30 nm) and large ($D_p = 5000$–$10{,}000$ nm) particles. Conversely, the nozzle has poor performance at intermediate to large sizes ($D_p \sim 1000$ nm), but the lens is very effective at this size. Therefore, aerodynamic lenses and a nozzle act in a complementary fashion over most of the D_p range from 15 to 10,000 nm (except for a "hole" in the range from 30 to 70 nm); and one might therefore expect that the inlet could generate a highly collimated particle beam over this entire range (except for the "hole").

The valley at $D_p \cong 40$ nm in Figure 9 is the "hole," or actually a range of D_p in which neither the nozzle nor the lens is particularly effective. Changes in either the lenses or the nozzle might be explored in an effort to fill this hole. Here, we have explored only the former. Obviously, incorporation of further lenses into the design might be one way to fill the valley. Unfortunately, additional lenses may be only marginally successful, because the added lenses would operate at higher pressures, under which conditions they are not very effective in collimating small particles. Furthermore, the addition of more lenses will increase the overall length of the inlet, which is often undesirable in a practical instrument. Therefore, alternatives are sought.

As shown in Zhang et al. (2002; Figure 11), cylindrical lenses produce a stronger contraction than thin disk lenses do. Therefore, the five-lens inlet (upwardly pointing triangles) is modified so that the first and the last lens are changed to cylindrical lenses, each with a length of 10 mm. The results (filled circles) in Figure 9 show that transmission of large particles is significantly improved. But, surprisingly, the results also show that the use of cylindrical lenses causes the valley around $D_p = 40$ nm to be even deeper. In an effort to understand the reason for this deterioration in performance for small particles, we have analyzed the behavior of the individual lenses that comprise the two inlets.

The contraction ratio of individual lenses has been calculated for both inlets (upwardly pointing triangles and filled circles in Figure 9), which are geometrically identical except for the shape of the first and fifth lenses. The results are plotted in Figure 11a versus D_p and in Figure 11b versus the local value of St. Filled symbols correspond to an inlet with only thin disk lenses (Inlet A). Open symbols correspond to an inlet in which the first and last lenses are cylindrical (Inlet B). The results are for particles which, far upstream of the lens, have a position given

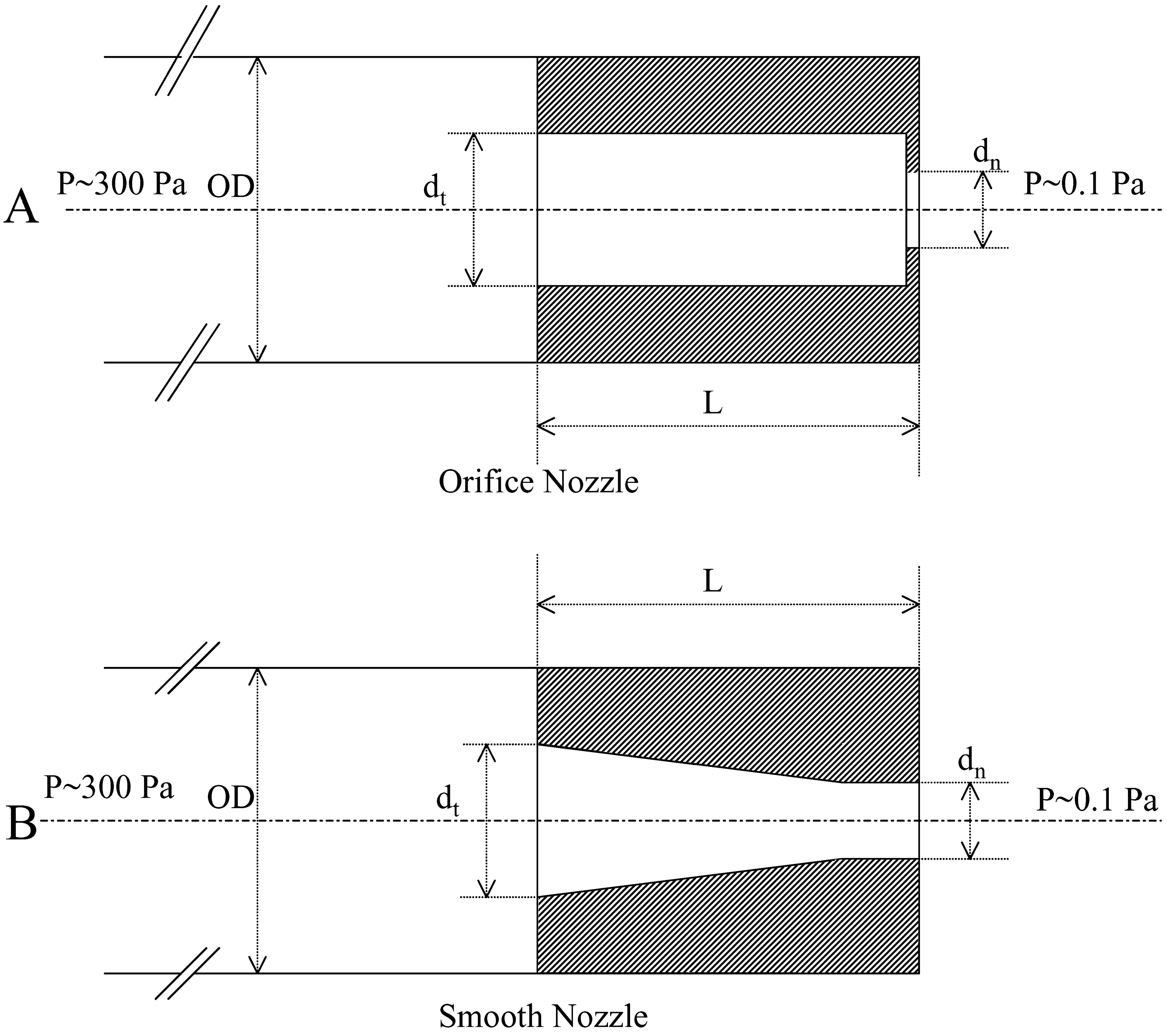

Figure 10. Geometrical configuration of two nozzles, OD = 10 mm, $d_t = 6$ mm, $d_n = 3$ mm, and L = 10 mm: (a) stepped nozzle, (b) smooth nozzle.

by $2R_{pi}/OD = 0.3$, the same as in Part I. One can see that, in the all-disk lens inlet (filled symbols), the lens contraction improves gradually from lenses 1 to 5 (Lens IDs from 5 to 4 mm). The results are consistent with those in Part I which show a similar effect with reductions in ID. As expected, Figure 11a shows that cylindrical lenses (lenses 1 and 5, open symbols) produced a stronger beam contraction, but the improvement is obvious only for particles with diameters greater than 35 nm. Results for lenses 2–4 in the two inlets are about the same, except that the dashed curves are shifted slightly to the right due to the effect of higher working pressures.

When the results are plotted versus St in Figure 11b, curves for lenses 2–4 in the two inlets coalesce because the lenses are identical. The results for lenses 1 and 5 of the two inlets are, of course, quite different. To understand the overall performance of the two inlets around the first valley in Figure 9 (D_p ~35 nm), results for the individual lenses at that particle diameter are summarized in Table 1.

Table 1 shows that contraction ratios for the first and fifth lenses are very close for the two inlets. One reason is that the two cylindrical lenses in Inlet B show a very limited improvement in contraction ratio for small particles (Figure 11a). Another reason

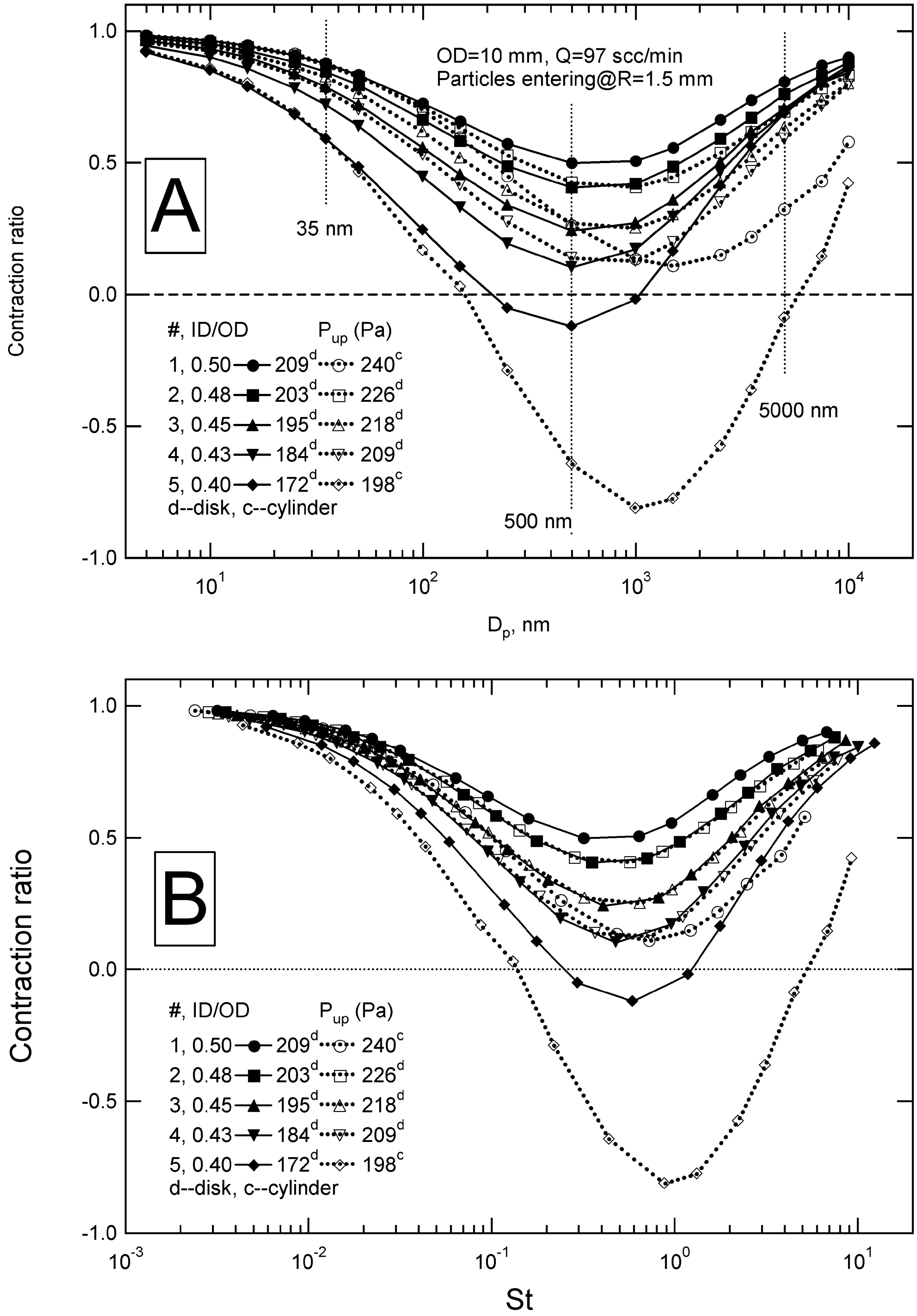

Figure 11. Contraction ratio of individual lenses for inlets A and B as described in Table 1. $2R_{pi}/OD = 0.3$. Filled symbols correspond to an inlet with only thin disk lenses (Inlet A). Open symbols correspond to an inlet in which the first and last lenses are cylindrical (Inlet B).

Table 1

Summary of lens contraction ratios and nozzle divergence angles for two inlets at $D_p = 35$ nm, $Q = 97$ scc/min, and OD = 10 mm lens

		1st	2nd	3rd	4th	5th	Total	Nzl. angle[+]	Char. angle[**]
A	ID/OD	0.5^d	0.48^d	0.45^d	0.43^d	0.4^d			
	Cont. ratio[*]	0.875	0.844	0.788	0.719	0.591	0.247	3.42	2.57
	P_{up}, Pa	209	203	195	184	172			
	St	0.022	0.025	0.029	0.034	0.041			
B	ID/OD	0.5^c	0.48^d	0.45^d	0.43^d	0.4^c			
	Cont. ratio[*]	0.875	0.869	0.825	0.775	0.589	0.286	3.42	2.93
	P_{up}, Pa	240	226	218	209	198			
	St	0.0168	0.0198	0.023	0.026	0.031			

A. Inlet for which all lenses are thin (0.5 mm) disks. Stepped nozzle as in Figure 11a, $D_t = 6$ mm, $d_n = 3$ mm, L = 10 mm.

B. Same as A, but first and fifth lenses are cylinders (length = 10 mm).

C, Cylindrical; d, disk.

[*] Contraction ratios are based on particles entering upstream of lenses at $2R_{pi}/OD = 0.3$.

[+] Nozzle angle (mrad) is based on particle entering upstream of nozzle at $2R_{pi}/OD = 0.1$.

[**] Characteristic angle (mrad) is based on particle entering upstream of inlet at $2R_{pi}/OD = 0.3$.

is that, for the same flow rate of about 97 scc/min, Inlet B operates at a higher pressure, and, hence, St for every lens component is smaller. Due to the smaller value of St, lenses 2–4 in Inlet B have worse performance than in Inlet A. Total contraction ratios are calculated by multiplying contraction ratios of lenses 1–5 in the respective inlets. The total contraction ratio is seen to be worse for Inlet B. From the isolated nozzle results (Zhang et al. 2002) and the calculated radial coordinate of a particle downstream of the fifth lens, the particle divergence angle can also be calculated. This characteristic angle, which is given in the table, is larger for Inlet B than for Inlet A. This is consistent with the transmission results in Figure 9.

Characteristic angle results as calculated from the isolated component results are also plotted in Figure 12 versus particle diameter in order to facilitate comparison with those obtained by the integrated inlet calculation. Figure 12 shows that the two sets of results agree well for small particles, which indicates that one can use information for the isolated components to estimate performance of an integrated inlet in this region. The discrepancy for large particles in Inlet B is probably due to the fact that particles may not be fully relaxed onto the gas streamlines before entering the subsequent components in the integrated inlet. Based on trajectory analysis for a particle of $D_p = 5000$ nm, it is observed that, in Inlet B, the particle has a noticeable radial velocity toward the axis throughout the inlet, whereas in Inlet A the radial velocity immediately upstream of each lens is barely observable until the 4th lens.

Also, for large particles ($D_p > 5000$ nm), Figure 11 shows that every lens in Inlet B offers better collimation than its counterpart in Inlet A. Therefore, Inlet B should exhibit better performance for large particles. In Figure 12, this is reflected in a smaller characteristic angle for Inlet B. In Figure 9, it is reflected in an efficiency for large particles that approaches the ballistic limit.

Finally, the last curve (filled squares) in Figure 9 is the transmission efficiency for an inlet with a smooth nozzle (Figure 10b). This inlet is identical to that used by Jayne et al. (2000) except for the OD (10 mm versus 8.8 mm). Both nozzles shown in Figure 10 have the same overall dimensions, and the only difference is that the nozzle in Figure 10b has a smooth transition from d_t to d_n. Figure 9 shows that the smooth nozzle will not collimate particles smaller than about 50 nm. From single-nozzle results it is known that this is because onset of the axis-crossing phenomenon, which occurs at $D_p \cong 20$ nm in a stepped nozzle, is delayed until $D_p \cong 50$ nm in a smooth nozzle. Of course, there is now no valley at $D_p \cong 35$ nm because the nozzle does not start to be effective until $D_p \sim 50$ nm. Because the smooth nozzle requires a higher upstream pressure in order to maintain the same flow rate, incipient particle impact on the first lens is shifted from $D_p = 500$ nm to 650 nm.

Effect of Lens Inner Diameters. As shown in Figure 9, increasing the number of lenses to five and using cylindrical lenses does not fully remove the valley for small particles. Therefore, alternative approaches are sought to improve the collimation of small particles. As shown in Figure 10 of Zhang et al. (2002), smaller values of ID/OD improve the contraction coefficient for small particles, although most improvement is for intermediate to large particles. Nonetheless, the effect of lens ID/OD has been investigated.

As in Figure 9, Q was set equal to 97 scc/min and the OD was taken to be 10 mm. In order to improve collimation of small particles, the diameter of the last lens was reduced slightly (from 4 mm to 3.5 mm). The stepped nozzle shown in Figure 10a was used. The inner diameter (ID) of the lenses varies linearly from the first to the last. Figure 13 shows the particle transmission efficiency (after considering Brownian motion) for the inlets in which the ID of the first lens varies from 6.5 to 3.5 mm. The results are considerably better than those given in Figure 9.

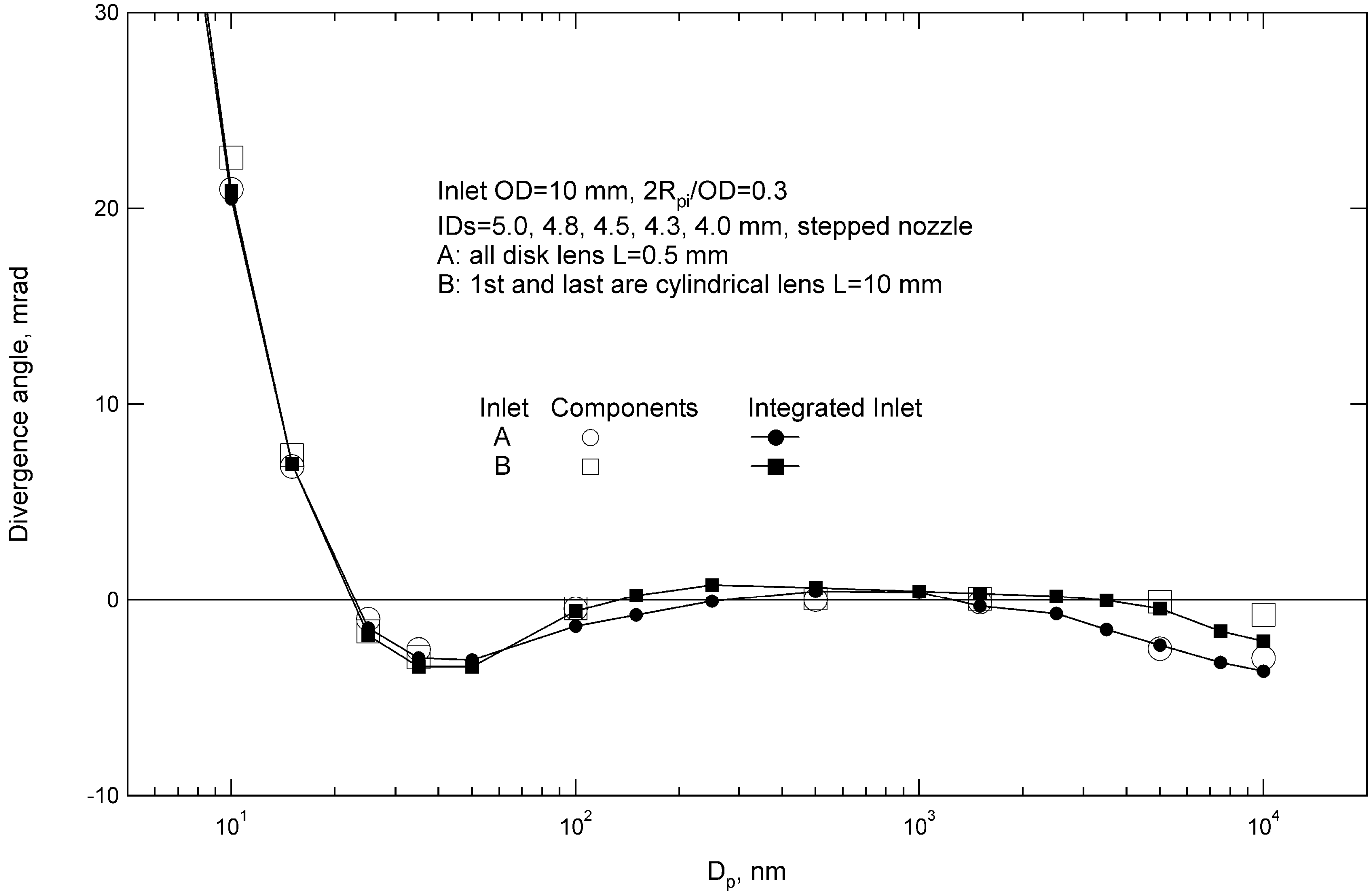

Figure 12. Beam divergence angle for particle entering upstream of two different inlets. $2R_{pi}/OD = 0.3$ for both cases. Integrated inlet: calculated for intact system. Components: calculated from performance of isolated components (lenses and nozzle). Inlets A and B as described in Table 1.

In fact, with the first lens ID = 4.5 or 3.5 mm, the valley at 35 nm is fully removed. This is a consequence of the dependence of the contraction ratio on ID/OD. As discussed in previous sections, the loss of large particles ($D_p > 400$ nm) shown in Figure 13 is due largely to impact of particles on surface of the first lens. However, it is observed that the losses are surprisingly large for the inlets with ID = 6.5 and 5.5 mm. This is simply because these two inlets do not collimate large particles very well. As a result, the beam divergence angle is large and some large particles do not impact on the detector. By contrast, for the inlets for which the ID of the first lens is either 3.5 or 4.5 mm, the large particles are collimated so well that transmission is fully controlled by impact on the first lens. The figure shows that, even after considering Brownian broadening, transmission exceeds 50% for all particles between D_p = 20–1000 nm. In addition, it is seen that the usual practice of varying the lens ID from the first to the last is probably unnecessary and perhaps even unwise. Note that a design with constant ID offers machining convenience.

Collimation of Ultrafine Particles. In studies of new particle formation, there is a need to measure ultrafine particles ($D_p \sim 10$ nm). Figure 13 gives transmission results for designs that work well for D_p = 20–1000 nm, and they work reasonably well up to D_p = 10,000 nm (~40% transmission efficiency). The major difficulty, however, appears at the small particle end as the transmission efficiency falls sharply almost to zero for $D_p < 15$ nm.

As suggested earlier, the dominant element for the collimation of very small particles is the nozzle. More specifically, aerodynamic collimation is achieved at a nozzle Stokes number of about one, but the Stokes number for very small particles is usually much less than one. Based on the definition of St for a nozzle, an accurate approximation for small particles is

$$\mathrm{St} \propto \frac{D_p}{d_n}\frac{1}{P_{up}}. \qquad [5]$$

Therefore, one can improve transmission of very small particles either by reducing the nozzle throat diameter d_n while maintaining P_{up} constant or by reducing P_{up} while maintaining d_n constant. In either case, the consequences will be measured relative to an inlet with all IDs = 3.5 mm as represented by the circles

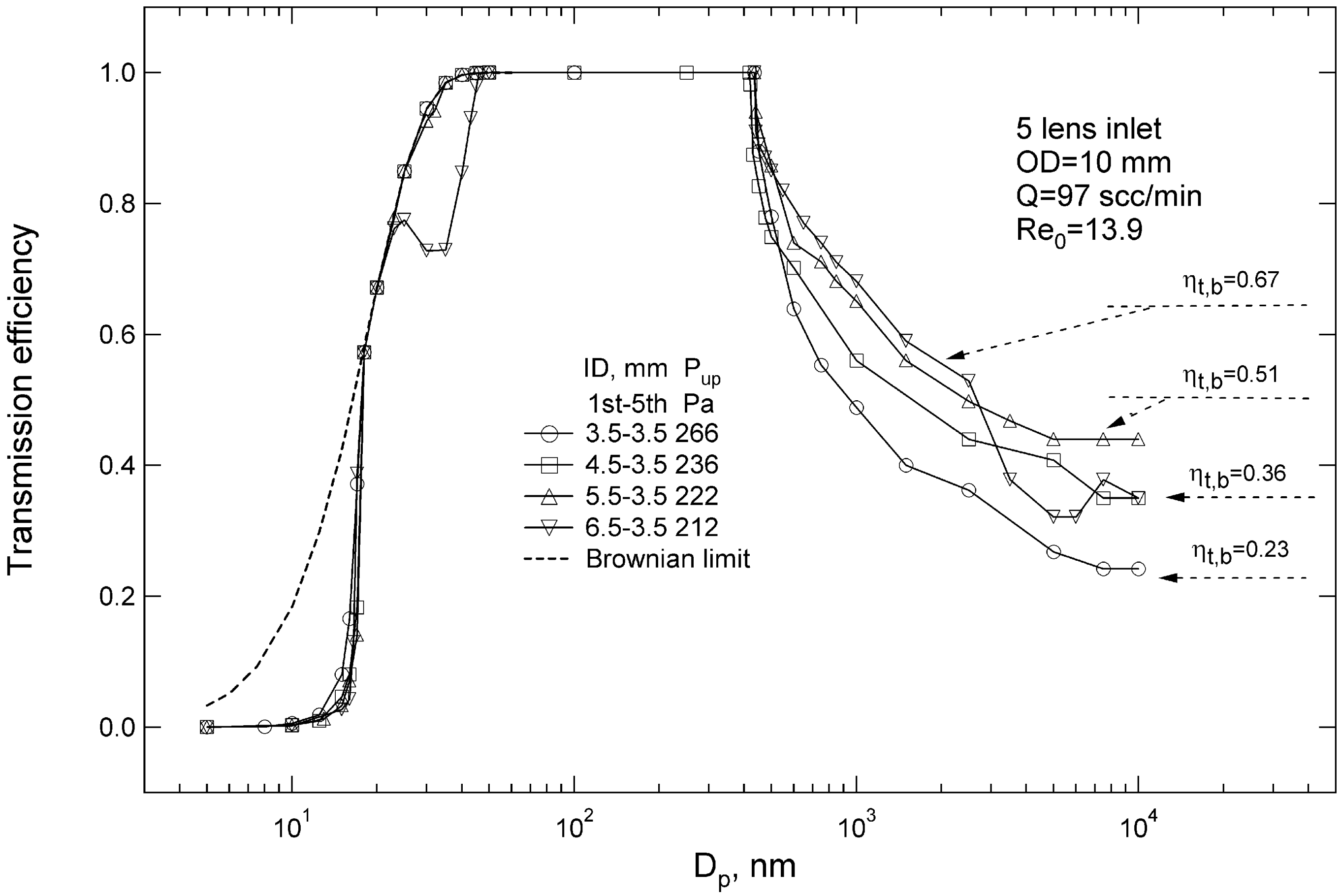

Figure 13. Influence of lens IDs on particle transmission efficiency. OD = 10 mm, Q = 97 scc/min, P_{back} = 0.1 Pa, stepped nozzle (Figure 10a), and Re_0 = 13.9. All lenses are thin (0.5 mm).

in Figure 13. Because this lens will serve as a base case, the performance of its individual components has been evaluated.

Contraction ratios for 5 individual lenses are shown in Figure 14a versus D_p and in Figure 14b versus St. Since all of the lenses are geometrically identical and operate at the same Re, Figure 14a shows that the curves are very similar but shift to smaller sizes from lenses 1 to 5 as operating pressure goes from 264 to 181 Pa. When plotted versus St in Figure 14b, the five curves fall on a nearly universal curve, similar to those shown in Zhang et al. (2002). The minor deviation of lens 1 from the rest is probably due to a difference in the flow field upstream of the lenses. It is found that flow upstream of lens 1 is fully developed, but the flows upstream of lenses 2–5 are not quite fully developed. Comparison of the curves in Figure 14 with those in Figure 11 indicates that, as expected, lenses with ID/OD = 0.35 produce a stronger effect. In particular, for a thin lens and $D_p \approx 1000$ nm, $\eta_c \cong -0.1$ for ID/OD = 0.4 and $\eta_c \cong -0.5$ for ID/OD = 0.35. Thus, the collimation is poorer in this particle range when ID/OD = 0.35. However, the collimation by the lenses has been improved for very small particles, and it is comparable for large particles.

To study the effect of reducing d_n at constant P_{up}, inlets were "constructed" by proportional reduction of axial and radial dimensions of the base inlet (ID/OD = 0.35) to 75% and 50% scale models. The particle transmission results for the inlets with reduced d_n are plotted in Figure 15 as upward pointing triangles (75% of the base inlet) and downward pointing triangles (50% of the base inlet). The open symbols are for purely aerodynamic collimation, and the filled symbols are for purely Brownian broadening. As expected, for purely aerodynamic collimation the transmission efficiency plotted in Figure 15 shows that the cutoff D_p for small particles roughly scales with d_n. For instance, a reduction in d_n by 50% from 3 to 1.5 mm reduces the D_p at which η_t departs from unity from 18 to 9 nm. However, Figure 15 also indicates that Brownian motion represents a major obstacle to the collimation of ultrafine particles. Furthermore, the figure shows that Brownian motion is even worse after the reduction in inlet dimensions. This is because the terminal velocity of very fine particles decreases with reductions in nozzle dimensions, whereas the distance from the nozzle to the target was not scaled down. In other words, because the particle Stokes number is larger due to the reduction in dimensions, the

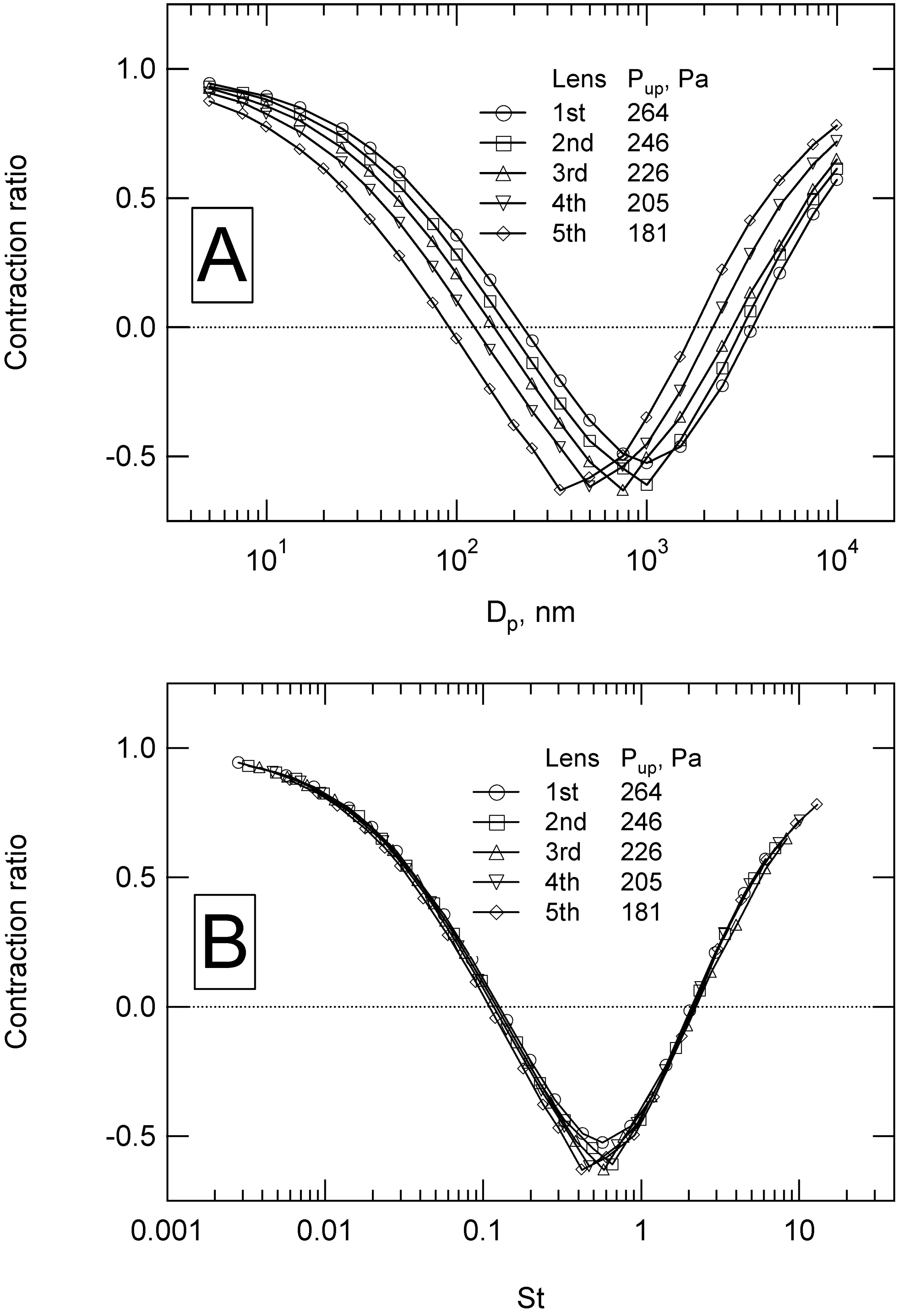

Figure 14. Performance of individual lenses for constant ID case in Figure 13 (circles). OD = 10 mm, Q = 97 scc/min, ID/OD = 0.35, $Re_0 = 13.9$, $2R_{pi}/OD = 0.3$. Stepped nozzle.

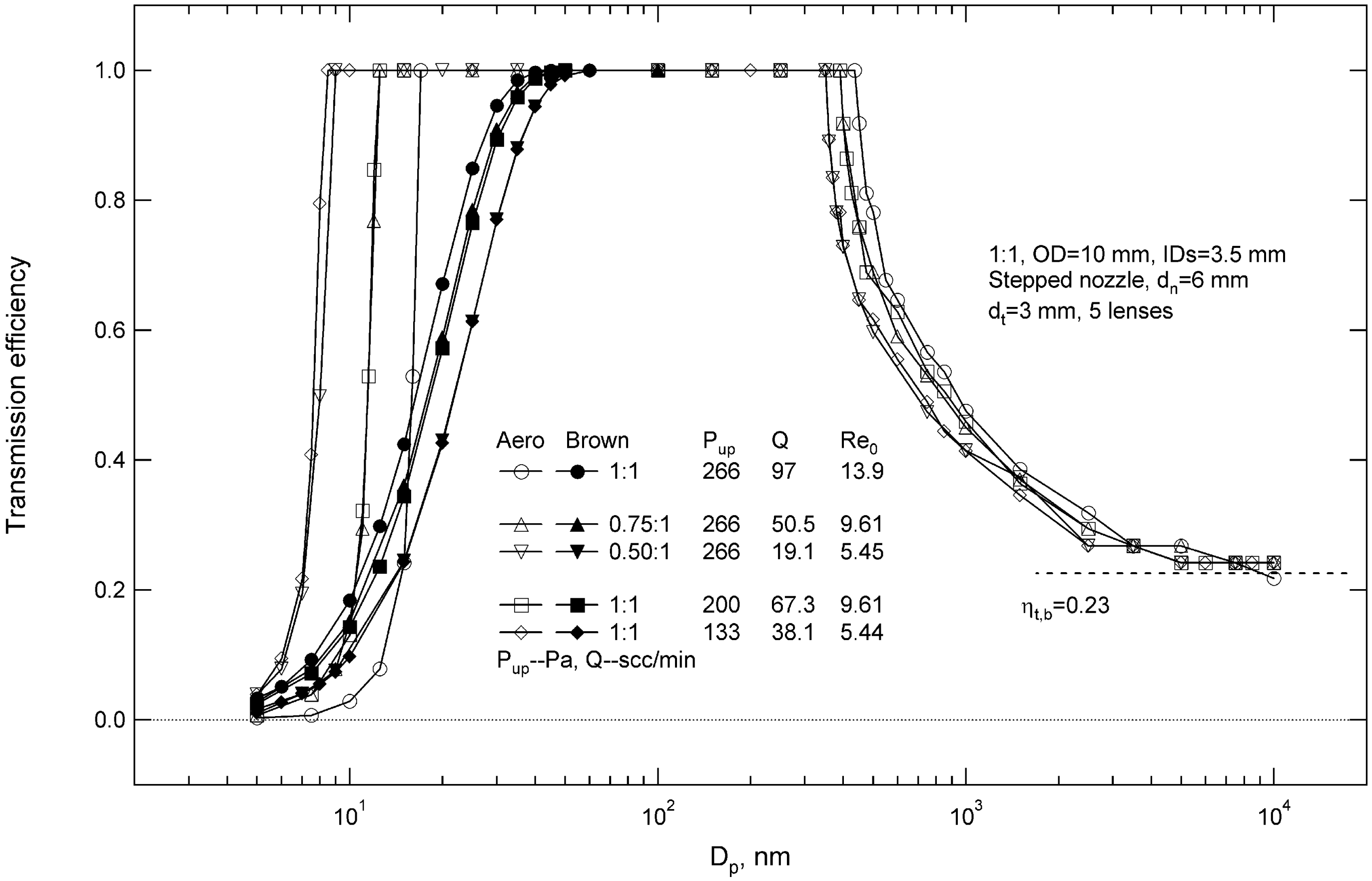

Figure 15. Transmission efficiency (purely aerodynamic) and Brownian limit for inlets which are geometrically similar.

particles follow the gas less closely. This has two contradictory effects on the particle beam. On the one hand it leads to better collimation. On the other hand, particles have lower terminal velocities. Hence, better aerodynamic collimation exacerbates Brownian broadening.

Figure 15 shows that collimation of very small particles can also be improved by operating at a lower pressure (P_{up}). The results indicate that aerodynamic and Brownian transmission efficiencies for operation at 75% of the base pressure (266 Pa) are identical to those for an inlet with dimensions that are 75% of the base case but operated at the base operating pressure (266 Pa). The same result is found for a 50% reduction in P_{up} versus a 50% reduction in dimensions. The results provide numerical confirmation of Equation (5), which suggests that, in terms of particle transmission efficiencies (either aerodynamic or Brownian), the effects of d_n and P_{up} are identical. One can use either an inlet of smaller dimensions or operate the inlet at lower pressure to preferentially collimate smaller particles, or vice versa. Figure 15 further suggests that the base case inlet offers a roughly optimized balance between aerodynamic collimation and Brownian broadening. In other words, efforts to shift the low cutoff D_p to smaller values are not very successful because the Brownian broadening becomes worse. The efforts are worthwhile only if one really wants to collimate at least a few small particles. For example, for 10 nm particles, overall transmission efficiency for the base case is 0.005; whereas, with the reduction of either P_{up} or d_n to 75% of its base value, transmission efficiency is improved to 0.02.

As discussed, in terms of particle transmission efficiencies (either aerodynamic or Brownian), the effects of d_n and P_{up} are essentially identical, although there must be a small Reynolds number effect that is not apparent in the results. However, in terms of sampling rate, the effects of d_n and P_{up} are not identical. For example, a 50% reduction in pressure reduces the mass flow rate by a factor of only 2.5, but a 50% reduction in the inlet dimensions (d_n and OD) reduces the mass flow rate by a factor of 5. Therefore, the pressure adjustment scheme is preferred if one wants to collimate smaller particles. By the same rationale, if we wish to increase the sampling rate, it is better to increase OD than to increase P_{up} by the same factor. For instance, if P_{up} is increased by a factor of 2, Q increases by a factor of about 2.5. However, if OD is doubled, Q increases by factor of 5. Note that raising the flow rate either by using higher P_{up} or larger d_n will be at the expense of the low cutoff D_p. Fortunately, an appropriate adjustment of both P_{up} and the inlet dimension could increase flow rate and yet maintain the low cutoff D_p constant.

For example, one could increase the inlet dimensions by a factor of 2 but decrease P_{up} by 50%; the outcome is that Q is doubled and the low cutoff D_p is kept constant. From the experimental point of view, if St or Q is changed by moving to a different P_{up}, this requires only that a different pinhole be installed. If it is changed by moving to a different d_n, and if geometric similarity is to be preserved, as in this study, a new pinhole and a new inlet must be installed. Obviously, the former is much easier to implement. However, it should be noted that preservation of geometric similarity may not be important in some practical systems.

CONCLUSIONS

As a sequel to our previous effort on modeling particle motion through a single lens or nozzle (Zhang et al. 2002), particle motion in flows of gas–particle suspensions through an integrated aerodynamic-lens–nozzle inlet has been investigated numerically.

We found that in a five-lens inlet with a nozzle, 2/3 of the total pressure drop occurs at the final nozzle expansion and that the gas speed reaches about twice sonic in the nozzle expansion. Except for very large particles ($D_p > 2500$ nm), particles are accelerated and decelerated in each lens spacing and acquire a nearly constant velocity downstream of the nozzle expansion.

The inlet has a transmission efficiency (η_t) of unity for particles of intermediate diameter ($D_p \sim 30$–500 nm). The transmission efficiency is reduced to ~40% for large particles ($D_p > 2500$ nm) as a result of impact losses on the surfaces of the first lens. There is a catastrophic reduction of η_t to almost zero for very small particles ($D_p \leq 15$ nm). In addition, particle Brownian motion is a significant contributor to the catastrophic reduction of η_t at small D_p. It is found that overall particle transmission can be roughly calculated as the product of purely aerodynamic transmission and Brownian transmission.

The cutoff of particle transmission for very small particles is mainly controlled by nozzle geometry and operating conditions. One can use a particle Stokes number based on parameters that are appropriate to nozzle flow (inlet upstream pressure and sonic speed, and nozzle throat diameter, d_n) to find the location of the D_p cutoff, by applying St ~1 as a criterion. Furthermore, one can therefore use lower P_{up} or an inlet of small dimensions to preferentially sample small particles, or vice versa. By contrast, the particle transmission efficiency at intermediate diameters is mainly controlled by the lenses. Therefore, one can adjust nozzle geometry to shift the small particle cutoff, whereas adjustments in lens geometry (mainly ID/OD) or the use of more lenses can improve particle transmission at intermediate sizes. The results provide guidance on construction of an inlet with the desired beam performance based on the results for isolated lenses or nozzles provided in Part I (Zhang et al. 2002).

As examples, this article shows that, by using different lenses and nozzle, one can configure an inlet for preferentially sampling large particles (with $\eta_t > 50\%$ for $D_p = 50$–2000 nm). The inlet consists of five lenses separated by 50 mm with OD = 10 mm and IDs = 5.0*, 4.8, 4.5, 4.3, and 4.0* mm. A smooth nozzle as shown in Figure 10a is used. Note that the first and the last lenses (with * above) are cylindrical lenses with length of 10 mm, and all others are thin disks of 0.5 mm thickness. One can also configure an inlet of five thin disk lenses for sampling small particles (with $\eta_t > 50\%$ for $D_p = 20$–1000 nm). The thin disk lenses are of OD = 10 mm, IDs = 4.5, 4.2, 4.0, 3.8, and 3.5 mm and are separated by 50 mm. The nozzle is the stepped type as shown in Figure 10b. Some of the results have been compared with experimental data; and reasonable agreement has been found.

REFERENCES

Jayne, J. T., Leard, D. L., Zhang, X., Davidovits, P., Smith, K. A., Kolb, C. E., and Worsnop, D. R. (2000). Development of an Aerosol Mass Spectrometer for Size and Composition Analysis of Submicron Particles, *Aerosol Sci. Technol.* 33:49–70.

Liu, P., Ziemann, P. L., Kittelson , D. B., and McMurry, P. H. (1995a). Generating Particle Beams of Controlled Dimensions and Divergence: I. Theory of Particle Motion in Aerodynamic Lenses and Nozzle Expansions, *Aerosol Sci. Technol.* 22:293–313.

Liu, P., Ziemann, P. L., Kittelson, D. B., and McMurry, P. H. (1995b). Generating Particle Beams of Controlled Dimensions and Divergence: II. Experimental Evaluation of Particle Motion in Aerodynamic Lenses and Nozzle Expansions, *Aerosol Sci. Technol.* 22:314–324.

Shapiro, A. H. (1953). *The Dynamics and Thermodynamics of Compressible Fluid Flow*, Volume I, The Ronald Press Company, New York.

Tobias, H. J., Kooima, P. M., Dochery, K. S., and Ziemann, P. J. (2000). Real-Time Chemical Analysis of Organic Aerosols Using a Thermal Desorption Particle Beam Mass Spectrometer, *Aerosol Sci. Technol.* 33:170–190.

Zhang, X., Smith, K. A., Worsnop, D. R., Jimenez, J., Jayne, J. T. and Kolb, C. E. (2002). Numerical Characterization of Particle Beam Collimation by Aerodynamic Lens-Nozzle System: Part I: An Individual Lens or Nozzle, *Aerosol Sci. Technol.* 36:617–631.